Modelling the transport of geometrically necessary dislocations on slip systems: application to single- and multi-crystals of ice

Thiebaud Richeton, Lu Tuan Le, Thomas Chauve, Marc Bernacki, Stéphane Berbenni, Maurine Montagnat

Modelling the transport of geometrically necessary dislocations on slip systems: application to single- and multi-crystals of ice ‡

T Richeton[1], LT Le[1,2], T Chauve[3,4], M Bernacki[2], S Berbenni[1] and M Montagnat[3,4]

[1] Laboratoire d'Etude des Microstructures et de Mécanique des Matériaux (LEM3), UMR 7239, CNRS / Université de Lorraine, Ile du Saulcy, 57045 Metz, France
[2] MINES ParisTech, PSL - ResearchUniversity, CEMEF - Centre de mise en forme des matriaux, CNRS UMR 7635, CS 10207 rue Claude Daunesse 06904 Sophia Antipolis Cedex, France
[3] CNRS, LGGE, UMR 5183, 54 rue Molière, 38401 Grenoble, France
[4] Université Grenoble Alpes, LGGE, 54 rue Molière, 38041 Grenoble, France

E-mail: `thiebaud.richeton@univ-lorraine.fr`

Abstract. A model based on the elastic theory of continuously distributed dislocations that accounts for the transport of geometrically necessary dislocations (GND) on slip systems is developed. It allows keeping the crystallographic nature of glide by allocating velocities specific to slip systems to GND. At grain boundaries, the dislocation transport equation is resolved between a specific system in a grain and a specific system in the adjacent grain. It is used to simulate a compression creep test followed by unloading of a multiple slip deforming multi-crystal of ice during which kink band formation, grain boundary migration and localized grain nucleation are observed. The model predictions are compared to 2D strain fields obtained by digital image correlation and show a good agreement. Besides, the kink band position corresponds very well with an area of strong lattice misorientation predicted by the model and is also bounded by opposite densities of edge dislocations, in agreement with kink banding theory and characterization. Furthermore, the grain boundary migration is observed to happen from predicted low dislocation density area towards high dislocation ones, also in agreement with the theory. Lastly, the triple junctions where nucleation is observed are also characterized by high GND density and especially strong gradient of elastic energy density. These different features show the relevance of using a continuum theory of polarized dislocations per slip system to study the onset of relaxation mechanisms like kink banding, grain boundary migration and grain nucleation and possibly to propose nucleation and migration criteria.

Keywords: field dislocation mechanics, geometrically necessary dislocations, kink band, ice, digital image correlation, recrystallization

‡ Modelling and Simulation in Materials Science and Engineering 25 (2017) 025010 (27pp), doi:10.1088/1361-651X/aa5341

1. Introduction

Ice Ih has a hexagonal crystallographic structure and its plasticity is extremely anisotropic with huge predominance of basal slip [1]. Strong gradients of plastic strain are therefore expected in polycrystals and accordingly large amount of geometrically necessary dislocations (GND) [2, 3]. The consideration of GND effects can be well captured by the elastic theory of continuously distributed dislocations that was initiated by Kröner [4] and others [5–7]. This theory deals with the Nye's dislocation density tensor $\boldsymbol{\alpha}$ [8] which is a measure of lattice incompatibility [9]:

$$\boldsymbol{\alpha} = -curl\boldsymbol{F}^{*^{-1}}, \tag{1}$$

with $\boldsymbol{F}^{*^{-1}}$ the inverse of the elastic part of the deformation gradient. Using the Stokes' theorem, it provides the resulting Burgers vector $\boldsymbol{b}$ of all dislocation lines threading a surface S delimited by a given contour C:

$$\boldsymbol{b} = \int_S \boldsymbol{\alpha}\boldsymbol{n}dS = -\oint_C \boldsymbol{F}^{*^{-1}}dx. \tag{2}$$

Hence, the measure of $\boldsymbol{\alpha}$ is scale dependent. It reflects the density of GND at a given scale. The elastic theory of continuously distributed dislocations was rethought some years ago by Acharya and co-workers in considering the permanent deformation arising due to dislocation motion through the so-called Field Dislocation Mechanics (FDM) theory [10, 11]. The FDM theory thus accounts for the evolution of Nye's tensor through the resolution of the Mura's transport equation [6, 10, 12]. The FDM theory is well suited to be applied at a fine scale of resolution where the dislocations population can effectively be represented by GND densities. At higher scale, one should consider the coupling of GND with statistically stored dislocations (SSD) [13–18]. SSD compensate each others to give net zero Burgers vector and $\boldsymbol{\alpha} = \boldsymbol{0}$. The coupling of GND and SSD can be considered in models called Phenomenological model of Mesoscopic Field Dislocation Mechanics (PMFDM) or Reduced PMFDM (RPMFDM) thanks to a spatial averaging procedure [13, 15]. RPMFDM disregards the uniqueness of the Stokes-Helmholtz orthogonal decomposition of the elastic distortion into compatible and incompatible parts, which is possible when the material is taken initially free of GND [15]. It was shown that (R)PMFDM can account for size effects in connection with plastic strain gradients [14, 16, 18]. Compared to more classical Crystal Plasticity (CP) models, the distribution of elastic fields and the kinematic hardening are modified in (R)PMFDM due to the building-up of a polarized dislocation microstructure [14, 17]. Given the polarized nature of GND densities, (R)PMFDM is also particularly relevant in dealing with complex loading paths, such as reverse loading, since it can model the annihilation of dislocations of opposite signs without having to prescribe additional rules [12, 16, 17, 19].

Until now, (R)PMFDM was applied by considering only the global dislocation density tensor $\boldsymbol{\alpha}$ at each material point. As a consequence, the plastic distortion rate due to GND was obtained by the cross product with a single dislocation velocity

vector, $\boldsymbol{\alpha} \times \boldsymbol{V}$ [13–18]. This setting is acceptable in case of single slip in a single crystal [13–16] or in FDM models, if nonlinear crystal elasticity is used to incorporate lattice periodicity and symmetry [11, 20]. However, (R)PMFDM uses standard linear elasticity and the crystallographic character of plasticity is partially lost in multiple slip situations [17, 18]. In particular, dislocation velocity depends on the resolved shear stress and thus GND should not glide in the same way whether they are located on a highly or weakly stressed system. In strongly anisotropic materials like those with hexagonal structure, the crystallographic nature of plasticity is even more crucial since plastic deformation takes place by glide on slip families with different properties and notably different critical resolved shear stresses.

Actually following the original development of Acharya [10, 11], the present paper deals with RPMFDM where Nye's tensor is decomposed into edge and screw components on slip systems. This setting enables to allocate GND velocities specific to their slip system and eventually to their edge or screw character. Several approaches dealing with edge and screw densities on slip systems were already developed in the literature [21–27]. In the approach of [25, 26], GND are assumed to contribute to the hardening of the material but not to its plastic flow, meaning that all GND are deemed immobile. In [22–24], the generation of SSD is accounted for through the expansion of rectangular dislocation loops with edge and screw sides. This setting ensures the continuity of dislocation lines and the conservation of Burgers vectors. Furthermore, Arsenlis and co-workers [22, 23] make the distinction between positive and negative densities and introduce the coupling with GND densities through the contribution of Nye's tensor to the increment of positive and negative edge and screw densities on each slip system. In [23], the expression of Nye's tensor is different from (1) and leads to a different evolution equation as the one used in the present work (see thereafter (26)). Other authors have also been interested been in the continuous modeling of dislocations transport [27, 28]. For instance, in [27], a kinematic theory of plasticity is developed which comes off to an evolution equation that depends on four internal variables per slip system: total dislocation density, edge and screw GND densities and dislocation curvature density. A strong benefit of such theory is that it can account for line tension effects associated with dislocation curvature [27]. The aforementioned models that take into account the evolution of Nye's tensor were exclusively applied to simple or idealized cases, like single crystals [22, 23, 25, 27, 28] or bicrystals [26] and most often in single slip situations.

The present work deals with the application of a continuum theory of polarized dislocations per slip system to solve the dynamic problem of a multiple slip deforming multi-crystal with change of loading path. Hence, the issue of the transport of GND densities from a slip system in a grain to another slip system in an adjacent grain is tackled, albeit in a first simplified approach. Besides, the material is ice and given its strong plastic anisotropy [1], only GND densities on basal slip systems are considered. The paper outline is as follows. Notation conventions are settled in section 2. The equations of the model are described in section 3.1 while their numerical implementation

is detailed in section 3.2. The experimental procedure is briefly indicated in section 3.3. The identification of the model parameters is explained in section 4.1. In sections 4.2 and 4.3, the model is respectively used to simulate forward and reverse torsion creep curves of two ice single crystals with different sizes and temperatures, as well as the creep behavior of a multi-crystal of ice for which the 2D strain field is followed by Digital Image Correlation (DIC). Characterization of $\boldsymbol{c}$-axis orientations before and after the test is also performed, which allows identifying kink band formation, grain boundary migration and grain nucleation. Ice can indeed be considered as a model material to study these relaxation phenomena since they appear at very small strains ($\sim 1\%$) [29,30]. It is expected that accurate estimate of the internal stress level and of the dislocation distribution may allow progressing in their understanding [29, 30]. The outputs of the simulation are accordingly used to discuss the onset of these mechanisms, as well as the account of kinematic hardening in section 5. Concluding remarks follow in section 6.

2. Notations

Matrices and tensors are written in boldface type. The Einstein summation convention over repeated indices is used but summations over crystallographic slip systems are indicated explicitly. A superimposed dot denotes a time derivative. Standard notations are used with $\otimes$ the tensorial product, : the double contracted product between two tensors, $\times$ the cross-product, ∂, *grad*, *div* and *curl* the differential, gradient, divergence and curl operators, *det* and *tr* the determinant and trace of a matrix and $\|\|$ the magnitude of a vector. In particular, if $\boldsymbol{C}$ is a fourth-order tensor, $\boldsymbol{A}$ and $\boldsymbol{B}$ second-order tensors and $\boldsymbol{w}$ a vector, we have in rectangular Cartesian coordinates:

$$(Aw)_i = A_{ij}w_j, \tag{3}$$
$$(AB)_{il} = A_{ij}B_{jl}, \tag{4}$$
$$(curl\boldsymbol{w})_l = \in_{ljk} w_{k,j}, \tag{5}$$
$$(curl\boldsymbol{A})_{il} = \in_{ljk} A_{ik,j}, \tag{6}$$
$$(\boldsymbol{A} \times \boldsymbol{w})_{il} = \in_{ljk} A_{ij}w_k, \tag{7}$$
$$(\boldsymbol{C} : \boldsymbol{A})_{ij} = C_{ijkl}A_{kl}, \tag{8}$$

where $\in_{ljk}$ is a component of the third-order alternating Levi-Civita tensor $\boldsymbol{X}$.

3. Methods

3.1. Model

3.1.1. Finite strain Crystal Plasticity (CP) framework In the following, a finite strain CP formulation is presented in a condensed form. It follows the works of [31–34]. The deformation gradient $\boldsymbol{F}$ maps vectors of a stress-free reference configuration to

a deformed configuration. It is written according to the standard multiplicative decomposition:

$$\boldsymbol{F} = \boldsymbol{F^*}\boldsymbol{F^p}. \tag{9}$$

Stretching and rotation of the crystallographic lattice are included in $\boldsymbol{F^*}$. $\boldsymbol{F^p}$ denotes the plastic part of the deformation gradient which is assumed to leave the lattice unchanged. $\boldsymbol{F^p}$ is induced by glide on specific slip systems (s) characterized by their unit slip directions $\boldsymbol{b}^{(s)}$ and their unit slip plane normals $\boldsymbol{n}^{(s)}$. In the deformed configuration, the slip directions and the slip plane normals are, respectively, denoted $\boldsymbol{b^*}^{(s)}$ and $\boldsymbol{n^*}^{(s)}$ and are defined as follows:

$$\boldsymbol{b^*}^{(s)} = \boldsymbol{F^*}\boldsymbol{b}^{(s)}, \tag{10}$$
$$\boldsymbol{n^*}^{(s)} = \boldsymbol{n}^{(s)}\boldsymbol{F^{*-1}}. \tag{11}$$

$\boldsymbol{b^*}^{(s)}$ and $\boldsymbol{n^*}^{(s)}$ remain orthogonal but are not necessarily unit vectors anymore. The velocity gradient $\boldsymbol{L} = grad\boldsymbol{v} = \dot{\boldsymbol{F}}\boldsymbol{F^{-1}}$, with $\boldsymbol{v}$ the material velocity, can be split into an elastic and a plastic parts, $\boldsymbol{L^*}$ and $\boldsymbol{L^p}$ respectively:

$$\boldsymbol{L} = \boldsymbol{L^*} + \boldsymbol{L^p}, \tag{12}$$
$$\boldsymbol{L^*} = \dot{\boldsymbol{F}}^*\boldsymbol{F^{*-1}}, \tag{13}$$
$$\boldsymbol{L^p} = \boldsymbol{F^*}\dot{\boldsymbol{F}}^{\boldsymbol{p}}\boldsymbol{F^{p-1}}\boldsymbol{F^{*-1}}. \tag{14}$$

The plastic portion $\boldsymbol{L^p}$ is related to the slipping rate $\dot{\gamma}^{(s)}$ of slip systems (s) by:

$$\boldsymbol{L^p} = \sum_s \dot{\gamma}^{(s)}\boldsymbol{b^*}^{(s)} \otimes \boldsymbol{n^*}^{(s)}. \tag{15}$$

The tensors $\boldsymbol{L}$, $\boldsymbol{L^*}$ and $\boldsymbol{L^p}$ can be decomposed into symmetric (stretching) and skew-symmetric (spin) parts:

$$\boldsymbol{L} = \boldsymbol{D} + \boldsymbol{\Omega}, \tag{16}$$
$$\boldsymbol{L^*} = \boldsymbol{D^*} + \boldsymbol{\Omega^*}, \tag{17}$$
$$\boldsymbol{L^p} = \boldsymbol{D^p} + \boldsymbol{\Omega^p}. \tag{18}$$

For each slip system, the symmetric and the skew-symmetric orientation Schmid tensor are respectively introduced as:

$$\boldsymbol{R}^{(s)} = \frac{1}{2}\left(\boldsymbol{b^*}^{(s)} \otimes \boldsymbol{n^*}^{(s)} + \boldsymbol{n^*}^{(s)} \otimes \boldsymbol{b^*}^{(s)}\right), \tag{19}$$
$$\boldsymbol{S}^{(s)} = \frac{1}{2}\left(\boldsymbol{b^*}^{(s)} \otimes \boldsymbol{n^*}^{(s)} - \boldsymbol{n^*}^{(s)} \otimes \boldsymbol{b^*}^{(s)}\right). \tag{20}$$

Then, the tensors $\boldsymbol{D^p}$ and $\boldsymbol{\Omega^p}$ can be written as:

$$\boldsymbol{D^p} = \boldsymbol{D} - \boldsymbol{D^*} = \sum_s \boldsymbol{R}^{(s)} \dot{\gamma}^{(s)}, \tag{21}$$

$$\boldsymbol{\Omega^p} = \boldsymbol{\Omega} - \boldsymbol{\Omega^*} = \sum_s \boldsymbol{S}^{(s)} \dot{\gamma}^{(s)}. \tag{22}$$

Following [31], the Jaumann rate of Cauchy stress $\boldsymbol{\sigma}$ is the corotational stress rate on axes that rotate with the lattice, $\mathring{\boldsymbol{\sigma}}^* = \dot{\boldsymbol{\sigma}} - \boldsymbol{\Omega^*}\boldsymbol{\sigma} + \boldsymbol{\sigma}\boldsymbol{\Omega^*}$, and is related to the tensor of elastic moduli $\boldsymbol{C}$ by:

$$\mathring{\boldsymbol{\sigma}}^* + tr(\boldsymbol{D})\boldsymbol{\sigma} = \boldsymbol{C} : \boldsymbol{D^*}. \tag{23}$$

Static stress equilibrium without body forces is resolved for the Cauchy stress $\boldsymbol{\sigma}$:

$$div\ \boldsymbol{\sigma} = \boldsymbol{0}. \tag{24}$$

The resolved shear stress on a slip system, $\tau^{(s)}$, is defined such that the product $\tau^{(s)}\dot{\gamma}^{(s)}$ is the intrinsic dissipation associated to system (s) per unit reference volume [32–34]:

$$\tau^{(s)} = \boldsymbol{b^*}^{(s)} J\boldsymbol{\sigma}\boldsymbol{n^*}^{(s)}, \tag{25}$$

with $J = \det \boldsymbol{F}$ and $J\boldsymbol{\sigma}$ being the Kirchhoff stress.

3.1.2. Coupling with the transport of GND and constitutive assumptions Our material is assumed to be initially free of GND. The Nye tensor (1) is therefore updated at each time step through the resolution of the transport equation which gives the rate of GND density $\dot{\boldsymbol{\alpha}}$ [6, 10, 12, 13, 35]:

$$\mathring{\boldsymbol{\alpha}} = -curl\left(\boldsymbol{F^{*-1}}\boldsymbol{L^p}\right). \tag{26}$$

$\mathring{\boldsymbol{\alpha}}$ actually represents a convected derivative of $\boldsymbol{\alpha}$ following material elements which is obtained from Nanson's formula [10, 20]:

$$\mathring{\boldsymbol{\alpha}} = \dot{\boldsymbol{\alpha}} + (div\ \boldsymbol{v})\boldsymbol{\alpha} - \boldsymbol{\alpha}\boldsymbol{L^T}, \tag{27}$$

Given that our intention is to handle GND densities related to slip systems, (26) is re-written from (15) and (10) as [10]:

$$\mathring{\boldsymbol{\alpha}} = \sum_s -curl\left(\dot{\gamma}^{(s)}\boldsymbol{b}^{(s)} \otimes \boldsymbol{n^*}^{(s)}\right) = \sum_s \boldsymbol{b}^{(s)} \otimes curl\left(-\dot{\gamma}^{(s)}\boldsymbol{n^*}^{(s)}\right) = \sum_s \mathring{\boldsymbol{\alpha}}^{(s)}, \tag{28}$$

with the convected derivative of the GND density on slip system (s), $\boldsymbol{\alpha}^{(s)}$, given by:

$$\mathring{\boldsymbol{\alpha}}^{(s)} = \dot{\boldsymbol{\alpha}}^{(s)} + (div\ \boldsymbol{v})\boldsymbol{\alpha}^{(s)} - \boldsymbol{\alpha}^{(s)}\boldsymbol{L^T} = \boldsymbol{b}^{(s)} \otimes curl\left(-\dot{\gamma}^{(s)}\boldsymbol{n^*}^{(s)}\right). \tag{29}$$

Considering the unit vectors $\boldsymbol{b^{u*}}^{(s)} = \boldsymbol{b^*}^{(s)}/\|\boldsymbol{b^*}^{(s)}\|$, $\boldsymbol{n^{u*}}^{(s)} = \boldsymbol{n^*}^{(s)}/\|\boldsymbol{b^*}^{(s)}\|$ and $\boldsymbol{k^{u*}}^{(s)} = \boldsymbol{b^{u*}}^{(s)} \times \boldsymbol{n^{u*}}^{(s)}$ which corresponds to the tangent line direction of edge

dislocations on system (s) [23], $\boldsymbol{\alpha}^{(s)}$ can be related to the screw and edge GND densities on system (s) as follows:

$$\boldsymbol{\alpha}^{(s)} = \alpha_{screw}^{(s)} \boldsymbol{b}^{(s)} \otimes \boldsymbol{b}^{\boldsymbol{u}*(s)} + \alpha_{edge}^{(s)} \boldsymbol{b}^{(s)} \otimes \boldsymbol{k}^{\boldsymbol{u}*(s)}. \tag{30}$$

$\alpha_{screw}^{(s)}$ and $\alpha_{edge}^{(s)}$ hence represent dislocations whose true Burgers vectors point in the direction $\boldsymbol{b}^{(s)}$ in the intermediate configuration and whose lines are parallel to $\boldsymbol{b}^{u*(s)}$ and $\boldsymbol{k}^{\boldsymbol{u}*(s)}$ in the deformed configuration, respectively [10].

In the present model, it is assumed that GND cannot leave their slip system, *i.e.*, dislocation climb and cross-slip are disregarded in the transport equations (29) (see explanations in the Appendix). These mechanisms could be taken into account by considering out-of-plane motions in a more general transport equation for $\mathring{\boldsymbol{\alpha}}^{(s)}$ [11]. However, it is actually illusive to reproduce these elementary mechanisms through the transport equations (26) at the scale of our simulations which intend to model areas of several centimeters (mesh size $\sim 300\mu m$). Climb and cross-slip are nevertheless invoked to explain the multiplication of basal dislocations [36, 37]. Therefore, these phenomena are here indirectly taken into account through an evolution equation for the mobile statistical dislocation density $\rho_m^{(s)}$ [16, 38]:

$$\dot{\rho}_m^{(s)} = \left[\frac{C_1^{(s)}}{{b^{(s)}}^2} - C_2^{(s)} \rho_m^{(s)} \right] \left| \dot{\gamma}^{(s)} \right|, \tag{31}$$

where the mobile statistical dislocations multiplication is related to the parameter $C_1^{(s)}$ whereas $C_2^{(s)}$ characterizes mobile statistical dislocations annihilation. Furthermore, for the sake of simplicity, the same velocity magnitude $v^{(s)}$ is considered for all the dislocation species (screw, edge and mobile statistical dislocations) on a slip system (s), which is rather justified in ice for basal dislocations [39, 40]. Details of the derivation of $\dot{\gamma}^{(s)}$ are given in the Appendix. Its writing in the form of a classical Orowan relation (32) is obtained by assuming that the dislocation velocity is proportional to the projection of the driving force on the slip plane [11]:

$$\dot{\gamma}^{(s)} = \left(\rho_m^{(s)} b^{(s)} + \sqrt{{\alpha_{screw}^{(s)}}^2 + {\alpha_{edge}^{(s)}}^2} \right) v^{(s)}, \tag{32}$$

where $b^{(s)}$ is the Burgers vector magnitude. The average dislocation velocity on system (s), relative to the material, is assumed to depend on thermal activation and on the local resolved shear stress according to a power law relationship [41]:

$$v^{(s)} = v_0^{(s)} e^{-\frac{G}{kT}} \left| \frac{\tau^{(s)}}{\tau_c^{(s)}} \right|^{n^{(s)}} \text{sgn}\ (\tau^{(s)}), \tag{33}$$

where $v_0^{(s)}$ is a reference velocity that will be adjusted, k the Boltzmann's constant and G the activation energy related to temperature T. $n^{(s)}$ is the inverse of the dislocation velocity sensitivity of stress, $\tau^{(s)}$ the resolved shear stress (25) and sgn $(\tau^{(s)})$ the sign of $\tau^{(s)}$. $\tau_c^{(s)}$ stands for the critical resolved shear stress of slip system (s). It

should be noted that no phenomenological back-stress is introduced in (33) as is usually done in the constitutive flow rule of ice in order to reproduce loading path change [16,29]. $\tau_c^{(s)}$ is written as the sum of the lattice friction stress $\tau_0^{(s)}$ and an expanded Taylor relation that accounts for dislocation interactions between systems [42]:

$$\tau_c^{(s)} = \tau_0^{(s)} + \mu b^{(s)} \sqrt{\sum_l a^{(sl)} \rho_t^{(l)}}, \tag{34}$$

$a^{(sl)}$ denotes the interaction coefficient which is related to the strength of the interaction between system (s) and (l) [43, 44]. μ is the isotropic shear modulus. $\rho_t^{(l)}$ depicts the total dislocation density on system (l). It corresponds to the sum of the SSD (mobile and immobile) and GND densities on system (l):

$$\rho_t^{(l)} = \rho_m^{(l)} + \rho_f^{(l)} + \rho_{GND}^{(l)} \text{ with } \rho_{GND}^{(l)} = \frac{\sqrt{{\alpha_{screw}^{(l)}}^2 + {\alpha_{edge}^{(l)}}^2}}{b^{(l)}}. \tag{35}$$

Besides, the same formalism as the one derived in [43] in face-centered cubic (fcc) crystals is adopted concerning the evolution equation of the immobile SSD densities:

$$\dot{\rho}_f^{(s)} = \left[\frac{C_3}{b^{(s)}} \sqrt{\sum_{l \in forest} a^{(sl)} \rho_f^{(l)}} + \frac{C_4}{b^{(s)}} \left(\sqrt{a^{(ss)} \rho_f^{(s)}} + \sum_{l \in copl} \sqrt{a^{(sl)} \rho_f^{(l)}} \right) - C_5 \rho_f^{(s)} \right] \left| \dot{\gamma}^{(s)} \right|. \tag{36}$$

This formalism makes the distinction of the dislocation storage rate due to interactions between forest slip systems (junction formations pictured by constant C_3) and the storage rate due to self and coplanar interactions (constant C_4). The storage rate due to collinear interactions is not accounted for in (36) since such kind of interactions essentially produce annihilations [43]. Finally, the constant C_5 allows to describe dynamic recovery.

3.1.3. Transport at grain boundaries Glide on basal $(0001) < 11\bar{2}0 >$ (B), prismatic $(1\bar{1}00) < 11\bar{2}0 >$ (P) and pyramidal $(11\bar{2}2) < 11\bar{2}\bar{3} >$ (Py) slip families are taken into account [3, 45] but, as mentioned in the introduction, only GND densities on basal slip systems are considered. It is noteworthy that the resolution of the transport equations (29) naturally takes into account the intra-granular rotation of the crystal lattice through the update of $\boldsymbol{n}^{*(s)}$. The situation of transport is however more complex at grain boundaries though grain boundaries just correspond to strong variation of lattice orientation in the present model. For a given slip system in a grain, another system in the adjacent grain has to be chosen to resolve equation (29). This choice does not affect the value of $\mathring{\boldsymbol{\alpha}}$ but it modifies the values of $\mathring{\boldsymbol{\alpha}}^{(s)}$, *i.e.* the GND distribution on the different slip systems. For convenience, it has been chosen to resolve the transport equations for all basal slip systems labeled 1, whether in the same grain or not, and the same for basal slip systems labeled 2 and 3. Hence, a re-numbering of basal systems has been performed through the 12 hexagonal lattice equivalent rotations. In the present first simplified approach, this re-numbering is such that systems labeled 1 has always the highest (positive) initial Schmid factor among the three basal systems and systems

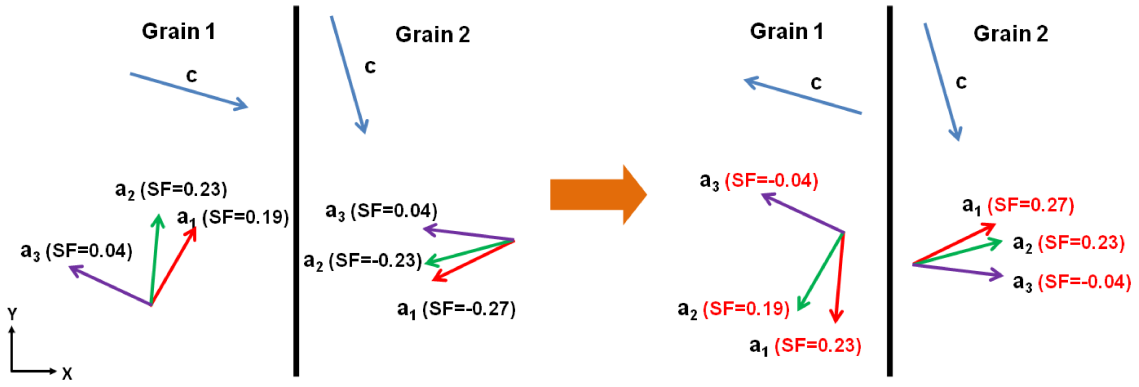

Figure 1. Scheme illustrating the re-numbering of basal slip systems in order to resolve the transport equations on slip systems at grain boundaries. The arrows represent the projections of the $\boldsymbol{c}$-axis and the 3 $\boldsymbol{a}$-axis of the hexagonal lattice in the global plane $(\boldsymbol{x}, \boldsymbol{y})$. SF denotes Schmid Factor. The values correspond to grain 1 and 2 of the compressed ice multi-crystal (see figure 3).

labeled 2 the second highest (positive) one (see figure 1). As a consequence, in all the grains, the initial resolved shear stresses are positive for systems labeled 1 and 2.

The current treatment is very simple and should clearly be improved in future work. For instance, slip systems involved in the resolution of the transport equations at grain boundaries could be better selected by following the geometrical criteria which were established experimentally for slip transmission [46–48]. It should be mentioned also that many different continuum approaches were already developed to handle the interactions between dislocations and grain boundaries [26, 49–55]. In [26] for instance, an additional resistance to slip, which is representative of the residual defect left at the boundary after transmission or absorption of a dislocation, is introduced in the flow rule in the vicinity of grain boundaries. The difficulty of such kind of approach lies in the width of the grain boundary influence zone since it is overestimated with mesh sizes practical for polycrystals. Many models, particularly within strain gradient crystal plasticity theories [49–55], therefore focus in specifying higher order boundary conditions at grain boundaries, which allow reducing the grain boundary to an interface layer. Strain gradient models involve however additional complexity due to the choice of phenomenological internal length scales. Impenetrable interfaces are commonly modeled with conditions corresponding to zero plastic distortion at grain boundaries [50, 52]. Coupling the behavior of adjacent grains can also be achieved by constraining the full continuity of plastic distortion accross the grain boundary [49, 54] or just the tangential part of it [17, 18, 35]. More complex frameworks include also the consideration of additional interface energy terms [51, 53, 55].

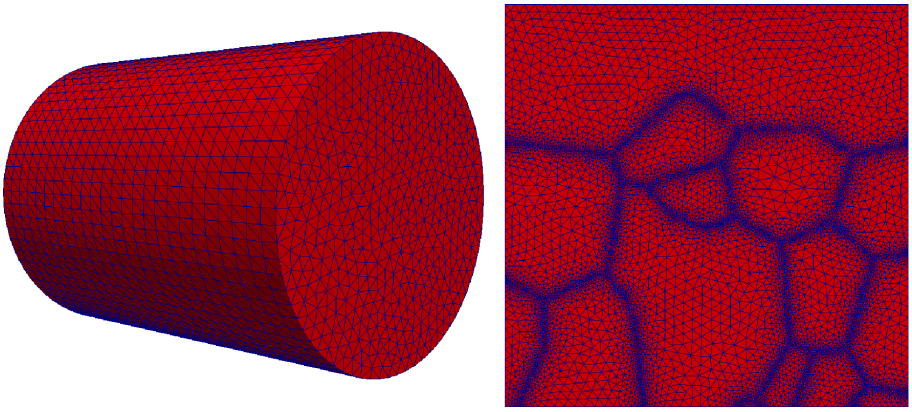

Figure 2. Unstructured FE mesh used in the simulations: single crystal A (left) with dimensions 46 mm (diameter) $*$ 50 mm (height) and multi-crystal (right) with dimensions 47.7 mm (height) $*$ 48 mm (width) $*$ 1.2 mm (thickness).

3.2. Numerical implementation

The model equations were numerically solved by the finite element method thanks to the use of the open source software *freefem++* [56]. Unstructured mesh made of 106152, 71400 and 70650 triangular P1 (linear) Lagrangian elements were used for meshing the multi-crystal, single crystal A and single crystal B, respectively (figure 2). For the multi-crystal, the initial regular mesh was remeshed to adapt to an isotropic geometric metric tensor field obtained from the error estimate corresponding to a compression test in anisotropic linear elasticity thanks to softwares *mshmet* and *mmg3d* present in *freefem++* [56].

A Newton-Raphson algorithm was used to maintain a constant applied torque (or force) from the rotation (or axial) velocity on the boundary in the torsion (or compression) creep tests, respectively. $\boldsymbol{D}$ and $\boldsymbol{\Omega}$ were computed from the material velocity $\boldsymbol{v}$ which derives from the equilibrium of $\boldsymbol{\sigma}$ (24). Following the rate tangent modulus method developed in [57], a linear interpolation within the time increment Δt was employed to define the slip increment on system (s):

$$\Delta\gamma^{(s)} = \Delta t \left[(1-\beta)\dot{\gamma}_t^{(s)} + \beta\dot{\gamma}_{t+\Delta t}^{(s)}\right], \tag{37}$$

where the time integration parameter $\beta = 0.5$. Besides, the approximation $J = 1$ is made in (25), meaning that the variation of mass density is neglected. It is noteworthy that this assumption implies $\|\boldsymbol{b}^{*(s)}\|\|\boldsymbol{n}^{*(s)}\| = 1$ in (15) and (25) and $div\ \boldsymbol{v} = 0$ in (27) and (29).

The transport equations were resolved following the explicit Galerkin/least squares formulation as introduced in [12]. It involves the adjonction of isotropic artificial diffusion terms in order to damp undesirable oscillations [12]. Therefore, at the small strain-rates investigated in the current simulations ($< 10^{-5}\mathrm{s}^{-1}$), the additional term of the finite strain form of the transport equations (27) ($\boldsymbol{\alpha}^{(s)}\boldsymbol{L}^{\boldsymbol{T}}$) is likely negligible compared to the diffusion term. In addition, a further simplification is made by resolving

each transport equation in the orthonormal frame $\left(\boldsymbol{b}^{\boldsymbol{u}*^{(s)}}, \boldsymbol{n}^{\boldsymbol{u}*^{(s)}}, \boldsymbol{k}^{\boldsymbol{u}*^{(s)}}\right)$ associated to its slip system and taking $\|\boldsymbol{n}^{*^{(s)}}\| = 1$. The resolution then reduces to two scalar equations for each basal slip system:

$$\dot{\alpha}^{(s)}_{screw} = \frac{\partial \dot{\gamma}^{(s)}}{\partial \boldsymbol{k}^{\boldsymbol{u}*^{(s)}}} = \frac{\partial \dot{\gamma}^{(s)}}{\partial \boldsymbol{x}} \frac{\partial \boldsymbol{x}}{\partial \boldsymbol{k}^{\boldsymbol{u}*^{(s)}}} + \frac{\partial \dot{\gamma}^{(s)}}{\partial \boldsymbol{y}} \frac{\partial \boldsymbol{y}}{\partial \boldsymbol{k}^{\boldsymbol{u}*^{(s)}}} + \frac{\partial \dot{\gamma}^{(s)}}{\partial \boldsymbol{z}} \frac{\partial \boldsymbol{z}}{\partial \boldsymbol{k}^{\boldsymbol{u}*^{(s)}}}, \tag{38}$$

$$\dot{\alpha}^{(s)}_{edge} = -\frac{\partial \dot{\gamma}^{(s)}}{\partial \boldsymbol{b}^{\boldsymbol{u}*^{(s)}}} = -\frac{\partial \dot{\gamma}^{(s)}}{\partial \boldsymbol{x}} \frac{\partial \boldsymbol{x}}{\partial \boldsymbol{b}^{\boldsymbol{u}*^{(s)}}} - \frac{\partial \dot{\gamma}^{(s)}}{\partial \boldsymbol{y}} \frac{\partial \boldsymbol{y}}{\partial \boldsymbol{b}^{\boldsymbol{u}*^{(s)}}} - \frac{\partial \dot{\gamma}^{(s)}}{\partial \boldsymbol{z}} \frac{\partial \boldsymbol{z}}{\partial \boldsymbol{b}^{\boldsymbol{u}*^{(s)}}}, \tag{39}$$

with $(\boldsymbol{x}, \boldsymbol{y}, \boldsymbol{z})$ the macroscopic rectangular Cartesian frame. The explicit Galerkin/least squares formulation then corresponds to:

$$\begin{aligned}
&\int_V \alpha^{(s)}_{screw}(t+\Delta t) w_1 dV = \int_V \alpha^{(s)}_{screw}(t) w_1 dV + \Delta t \int_V \frac{\partial \dot{\gamma}^{(s)}}{\partial \boldsymbol{k}^{\boldsymbol{u}*^{(s)}}} w_1 dV \\
&+ \frac{\Delta t^2}{1+\chi} \left(\int_V V_3^{(s)} \frac{\partial w_1}{\partial \boldsymbol{k}^{\boldsymbol{u}*^{(s)}}} \frac{\partial \dot{\gamma}^{(s)}}{\partial \boldsymbol{k}^{\boldsymbol{u}*^{(s)}}} dV + \int_V V_1^{(s)} \frac{\partial w_1}{\partial \boldsymbol{k}^{\boldsymbol{u}*^{(s)}}} \frac{\partial \dot{\gamma}^{(s)}}{\partial \boldsymbol{b}^{\boldsymbol{u}*^{(s)}}} dV \right) \\
&- \eta \Delta h^2 \int_V \left(\frac{\partial w_1}{\partial \boldsymbol{b}^{\boldsymbol{u}*^{(s)}}} \frac{\partial \alpha^{(s)}_{screw}}{\partial \boldsymbol{b}^{\boldsymbol{u}*^{(s)}}} + \frac{\partial w_1}{\partial \boldsymbol{k}^{\boldsymbol{u}*^{(s)}}} \frac{\partial \alpha^{(s)}_{screw}}{\partial \boldsymbol{k}^{\boldsymbol{u}*^{(s)}}} \right) dV,
\end{aligned} \tag{40}$$

$$\begin{aligned}
&\int_V \alpha^{(s)}_{edge}(t+\Delta t) w_2 dV = \int_V \alpha^{(s)}_{edge}(t) w_2 dV - \Delta t \int_V \frac{\partial \dot{\gamma}^{(s)}}{\partial \boldsymbol{b}^{\boldsymbol{u}*^{(s)}}} w_2 dV \\
&- \frac{\Delta t^2}{1+\chi} \left(\int_V V_1^{(s)} \frac{\partial w_2}{\partial \boldsymbol{b}^{\boldsymbol{u}*^{(s)}}} \frac{\partial \dot{\gamma}^{(s)}}{\partial \boldsymbol{k}^{\boldsymbol{u}*^{(s)}}} dV + \int_V V_3^{(s)} \frac{\partial w_2}{\partial \boldsymbol{b}^{\boldsymbol{u}*^{(s)}}} \frac{\partial \dot{\gamma}^{(s)}}{\partial \boldsymbol{b}^{\boldsymbol{u}*^{(s)}}} dV \right) \\
&- \eta \Delta h^2 \int_V \left(\frac{\partial w_2}{\partial \boldsymbol{b}^{\boldsymbol{u}*^{(s)}}} \frac{\partial \alpha^{(s)}_{edge}}{\partial \boldsymbol{b}^{\boldsymbol{u}*^{(s)}}} + \frac{\partial w_2}{\partial \boldsymbol{k}^{\boldsymbol{u}*^{(s)}}} \frac{\partial \alpha^{(s)}_{edge}}{\partial \boldsymbol{k}^{\boldsymbol{u}*^{(s)}}} \right) dV.
\end{aligned} \tag{41}$$

Δt is the time increment, w_1 and w_2 are test functions, V is the volume of the domain and Δh is the average length between adjacent nodes. $V_3^{(s)}$ and $V_1^{(s)}$ correspond, respectively, to velocities of screw and edge densities on slip system (s) (see (A.3) in the Appendix). These resolution schemes involve the use of three numerical parameters (table 1): χ which gives the weight of the Galerkin terms relative to least-squares terms, η an isotropic artificial diffusion factor and c the Courant number. The Courant condition for numerical stability established a maximum value for Δt:

$$\Delta t \leq c \frac{\Delta h}{v^{max}}, \tag{42}$$

where v^{max} is the maximal dislocation velocity among all slip systems. The values used for χ, η and c are given in table 1.

3.3. Experimental procedure

Two torsion creep tests of ice single crystals (A and B) oriented with their $\boldsymbol{c}$-axis parallel to the torsion axis [16, 58] were used as references to fit the model material

Table 1. Numerical parameters used in the resolution of the transport equations (unitless).

χ	η	c
1	0.01	0.15

parameters. The maximal applied shear stress was the same in both tests (0.1 MPa) but the temperature (A: $-10.5\,^{\circ}C$, B: $-13.5\,^{\circ}C$) and the sample's size (A: 46 mm (diameter) $*$ 50 mm (height), B: 30 mm $*$ 40 mm) were different. The applied torque was reversed after 5% and 4% of shear strain in tests A and B, respectively (see figure 4). Details of the experimental procedure can be found in [16,37,58]. Torsion tests on single crystals are ideal to calibrate the parameters of a (R)PMFDM model since the applied shear stress increases from the axis to the exterior of the sample, which generates a gradient of plastic distortion and thus significant GND density [16]. Moreover, the prediction of the reverse creep curves can only be achieved if annihilation of polarized dislocation densities is included in the model.

Besides, a multi-crystal of ice (15 grains) with rectangular shape ($48 * 47.7 * 12.1 mm^3$) (see figure 3) was specifically deformed in a cold room at $-4\,^{\circ}C$ under a compression creep stress of $0.25 MPa$ along the vertical axis until 1.9% of macroscopic strain and then unloaded. In order to reduce friction, the contact between the press and the sample was made through Teflon sheets. The lateral surfaces were stress free. The sample was cut from polycrystalline columnar ice elaborated following [29] such that the column axis was along the thickness of the sample. Hence, the sample contained one grain through the thickness and grain boundaries were almost perpendicular to the sample's surface. The $\boldsymbol{c}$-axis coordinates were measured over the entire sample's surface, before and after the test, using an optical Automatic Ice Texturer Analyser (AITA) [59]. The initial full lattice orientations of the grains were characterized in some representative areas by using Electron BackScatter Diffraction (EBSD) on the Crystal Probe Scanning Electron Microscope of Geosciences Montpellier (CNRS, University of Montpellier 2) mounted with a GATAN cold stage modulus (see details in [60]). During the test, 2D strain field measurements were obtained by DIC with a spatial resolution of $0.51 mm/pix$ (see details in [29]).

4. Results

4.1. Material parameters identification

Table 2 provides the parameters that are related to the ice crystal lattice, table 3 the values of the material parameters that are specific to slip families, table 4 those that are not specific and table 5 the interaction coefficients between slip systems. Contrary to previous simulations of ice crystals [3, 29, 45], $n^{(s)}$ does not represent the inverse of the strain rate sensitivity of stress but the inverse of the dislocation velocity sensitivity,

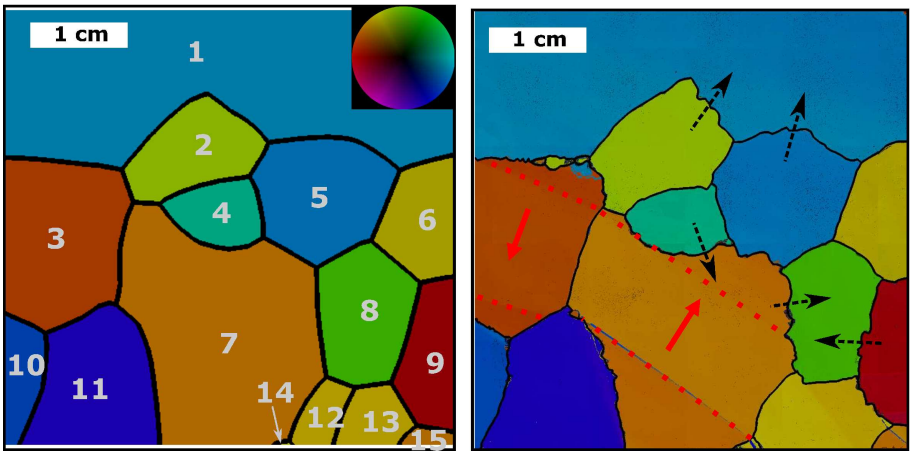

Figure 3. Specimen microstructure measured before and after deformation with the Automatic Ice Texturer Analyser (AITA). The angular color scale corresponds to the orientation of the $\boldsymbol{c}$-axis and is provided by the colorwheel. The dotted red lines indicate the presence of a kink band that crosses grains 3 and 7. The red arrows represent the projections of the first basal slip direction in the global plane $(\boldsymbol{x}, \boldsymbol{y})$. The dashed black arrows indicate the supposed directions of grain boundary migration.

Table 2. Parameters related to the ice crystal lattice at $-16°C$ [61].

$\boldsymbol{c/a}$	$\boldsymbol{b^{<a>}}$	$\boldsymbol{b^{<c+a>}}$	$\boldsymbol{\mu}$	
1.629	4.52 Å	8.63 Å	3.00 GPa	
$\boldsymbol{C_{11}}$	$\boldsymbol{C_{33}}$	$\boldsymbol{C_{44}}$	$\boldsymbol{C_{12}}$	$\boldsymbol{C_{13}}$
12.93 GPa	15.01 GPa	3.01 GPa	7.08 GPa	5.76 GPa

which can make a difference in case of strong evolution of the mobile dislocation density (see (32)). Hence, for basal slip, the value was not 2 but 1, in agreement with the linear relation observed between basal dislocation velocity and resolved shear stress [39, 40]. For the exponents of prismatic and pyramidal systems, the same values as those determined in [45] for strain-rate sensitivity were used since very low mobile dislocation multiplication were considered on these systems (there is no GND on non-basal slip systems and the value of the multiplicative constant C_1 (31) is eight times lower on non-basal slip systems compared to basal ones (see table 3)). A unique value of the activation energy G was used. It corresponds to the value measured in [40] for basal screw dislocations. The values of the basal-prismatic (a^{BP}) , prismatic-basal (a^{PB}) and prismatic-prismatic (a^{PP}) interaction coefficients associated with the formation of junctions, as well as the values of the strong basal-prismatic collinear interactions (a^{coli}) were those evaluated in [44] from dislocation dynamics simulations in ice single crystals. The coefficient for basal self-interaction (a^{BB}) was taken relatively high, following the recommendation of [44] that this coefficient may be considered as an effective self-interaction coefficient accounting for the strong interaction with collinear superjogs due to double cross-slip mechanisms. In [44] however, pyramidal-$< a >$ glide

Table 3. Model parameters that are specific to slip families. B: $(0001) < 11\bar{2}0 >$, P: $(1\bar{1}00) < 11\bar{2}0 >$, Py: $(11\bar{2}2) < 11\bar{2}\bar{3} >$.

	$\boldsymbol{B}$	$\boldsymbol{P}$	$\boldsymbol{Py}$
$\boldsymbol{\tau_0}$	0.04 MPa	0.1 MPa	0.5 MPa
$\boldsymbol{n}$	1	2.85	4
$\boldsymbol{C_1}$	$8 \cdot 10^{-9}$	$1 \cdot 10^{-9}$	$1 \cdot 10^{-9}$
$\boldsymbol{\rho_{f_0}}$	$1 \cdot 10^{6}\,\mathrm{m}^{-2}$	$1 \cdot 10^{5}\,\mathrm{m}^{-2}$	$1 \cdot 10^{5}\,\mathrm{m}^{-2}$
$\boldsymbol{\rho_{m_0}}$	$8 \cdot 10^{7}\,\mathrm{m}^{-2}$	$8 \cdot 10^{6}\,\mathrm{m}^{-2}$	$8 \cdot 10^{6}\,\mathrm{m}^{-2}$

Table 4. Model parameters that are not specific to slip families.

$\boldsymbol{v_0}$	$\boldsymbol{G}$	$\boldsymbol{C_2}$	$\boldsymbol{C_3}$	$\boldsymbol{C_4}$	$\boldsymbol{C_5}$
$1.2 \cdot 10^{8}\,\mathrm{ms}^{-1}$	0.76 eV	17	$2 \cdot 10^{-2}$	$1 \cdot 10^{-3}$	10

Table 5. Values of the interaction coefficients between slip systems (see text).

$\boldsymbol{a^{BP}}$	$\boldsymbol{a^{PB}}$	$\boldsymbol{a^{PP}}$	$\boldsymbol{a^{coli}}$	$\boldsymbol{a^{BB}}$	$\boldsymbol{a^{Py}}$
0.034	0.082	0.1	0.65	0.04	0.15

$(10\bar{1}1) < 11\bar{2}0 >$ was considered instead of pyramidal-$< c + a >$ $(11\bar{2}2) < 11\bar{2}\bar{3} >$, as done usually [3, 29, 45] and in the present work. As a consequence, a unique arbitrary value (a^{Py}) was considered for the interactions involving pyramidal systems (table 5).

The initial dislocation density in ice single crystals is estimated to be around $10^8\,\mathrm{m}^{-2}$ with a predominance of mobile dislocations [37]. ρ_{f_0} and ρ_{m_0} were adjusted accordingly with values ten times lower on non-basal slip systems compared to basal ones in order to allow for the strong plastic anisotropy of ice (table 3). The remaining material parameters (τ_0, v_0, C_1, C_2, C_3, C_4, C_5, a^{Py}) were first chosen by considering the values used in previous crystal plasticity models for ice [16, 29, 45] and then slightly adjusted to fit the mechanical response of the two torsion creep tests in ice single crystals described in section 3.3. For instance, our initial critical resolved shear stress for basal systems is a bit lower than in [16,29,45] due to the difference of viscosity ($n = 1$ compared to $n = 2$) but the ratios with prismatic and pyramidal systems are comparable to those in [29, 45]. In our formulation, the quantity $\rho_{m_0}^{(s)} b^{(s)} v_0^{(s)} e^{-\frac{G}{kT}}$ is equivalent to a reference slip rate. Its value, from $8 \cdot 10^{-9}\mathrm{s}^{-1}$ at $-13.5\,^{\circ}C$ to $2 \cdot 10^{-7}\mathrm{s}^{-1}$ at $-4\,^{\circ}C$, stands between the one used in [16] ($2 \cdot 10^{-10}\mathrm{s}^{-1}$) and the one used in [29, 45] ($10^{-6}\mathrm{s}^{-1}$). C_2 value is the same as in [16] whereas C_1 value is very close to the one used in [16] ($8 \cdot 10^{-9}$ compared to 10^{-8}). Following dislocation dynamics computations in fcc crystals [43], it seems sound to consider that constant C_3 which is associated with junctions formation should be higher than C_4 which is associated with self and coplanar interactions. Our C_3 and C_4 values are of similar magnitude order but lower than those found for fcc metals [43], meaning weaker isotropic hardening in ice than in metals. Finally, the value chosen for the constant C_5 corresponds to a typical initial annihilation distance of $5b$.

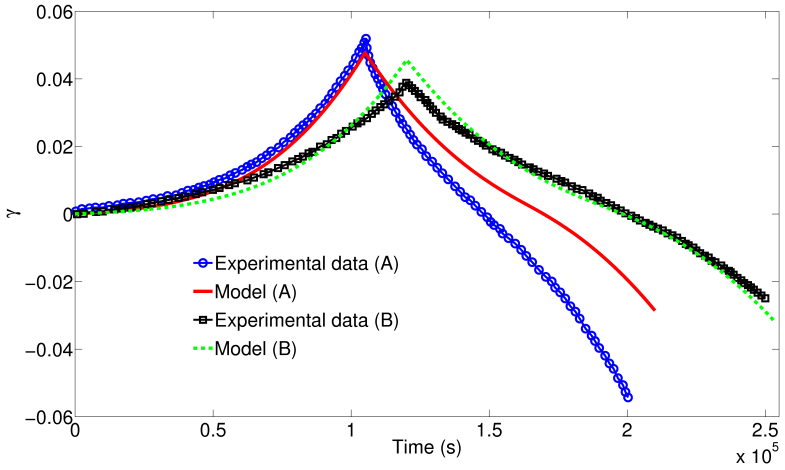

Figure 4. Experimental and simulated creep curves for single crystals A and B. γ represents the macroscopic torsion strain.

4.2. Torsion creep experiments of ice single crystals

Figure 4 compares the experimental and simulated creep curves for single crystals A and B. The acceleration of creep-rate during forward creep is interpreted as being caused by the multiplication of GND owing to the existence of a permanent deformation gradient in the sample. Experimental reverse creep curves display a slowing-down of the creep-rate which is followed by a re-acceleration. Such behavior is globally well reproduced with the present model although the mechanical behavior is very sensitive to initial conditions such as crystal orientation, temperature and dislocation density. Some disparity in these parameters might explain the discrepancy between the simulated and experimental creep curves. When the torque is reversed, GND with opposite sign as those formed during forward creep build up. These new GND thus annihilate with the GND of opposite sign present in the sample, leading to a complete decrease of the total GND density (figure 5). Then, a new GND microstructure, which is inversely polarized, arises and induces the re-acceleration of the reverse creep-rate. It is worth mentioning that single crystal B has actually a smaller radius than single crystal A. Hence, it displays a stronger GND production which involves softer behavior [16]. However, single crystal B is also deformed at a lower temperature, which involves harder behavior due to lower dislocation mobility (see (33)). This last effect is predominant since single crystal B exhibits a lower creep-rate.

4.3. Compression creep behavior of a multi-crystal of ice

4.3.1. Numerical simulation The multi-crystal compression creep test with an unloading after 1.9% of macroscopic axial strain was simulated using the present model. The simulated sample had dimensions $47.7 * 48 * 1.2mm^3$. Although some of the real grain boundaries displayed some deviations from orthogonality, grain boundaries were

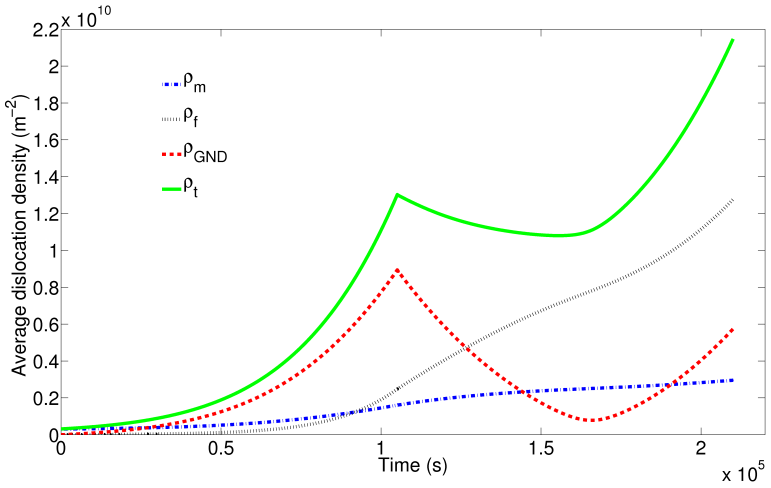

Figure 5. Evolution of the statistical mobile (ρ_m), immobile (ρ_f), GND (ρ_{GND}) and total (ρ_t) dislocation densities, summed over all slip systems and averaged over the specimen, during torsion creep of single crystal A.

Table 6. Initial statistical dislocation densities used for the simulation of the multi-crystal.

	$\boldsymbol{B}$	$\boldsymbol{P}$	$\boldsymbol{\Pi_2^{<c+a>}}$
$\boldsymbol{\rho_{f_0}}$	$1 \cdot 10^8\,\mathrm{m}^{-2}$	$1 \cdot 10^7\,\mathrm{m}^{-2}$	$1 \cdot 10^7\,\mathrm{m}^{-2}$
$\boldsymbol{\rho_{m_0}}$	$5 \cdot 10^8\,\mathrm{m}^{-2}$	$8 \cdot 10^7\,\mathrm{m}^{-2}$	$5 \cdot 10^7\,\mathrm{m}^{-2}$

taken perfectly perpendicular to the sample's surface. The same parameters as those used in the torsion of the two single crystals were considered, except for the initial SSD densities which were adjusted to get closer to the initial observed creep rate (see table 6). Initial dislocation densities in the multi-crystal might indeed differ from those in the single crystals due to different elaboration conditions. Moreover, in order to take into account friction, the dislocation velocity was slowed down at the top and bottom surfaces of the sample by multiplying the reference velocity $v_0^{(s)}$ (33) by a pre-factor. Different values were tested and the best compromise was obtained with a value of 0.1 which was applied during loading only. Because of the unknown friction and the fact that the top and bottom sample surfaces might be not perfectly parallel, this compression test was mechanically trickier to model than the torsion tests.

4.3.2. Macroscopic behavior and strain patterns Figure 6 exhibits the experimental and simulated macroscopic creep curves of the multi-crystal. Some discrepancy is clearly seen. The experimental creep rate is more or less constant whereas the simulation displays some creep acceleration before reaching a steadier rate. Moreover, the reverse strain jump at unloading is small compared the one measured. The continuously increasing macroscopic strain under zero load nevertheless shows that some

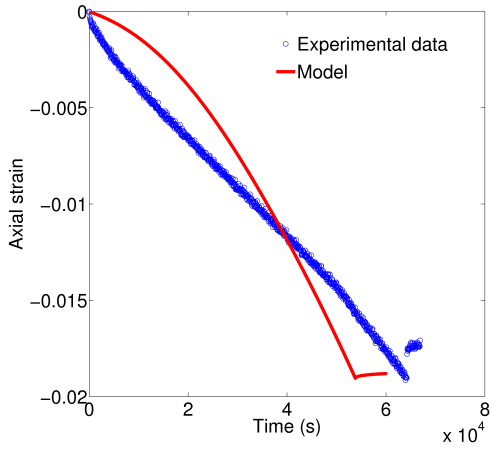

Figure 6. Experimental and simulated creep curve for the multi-crystal.

non negligible reverse plasticity occurred in the simulation.

Strain patterns ε_{yy}, ε_{xx} and ε_{xy} obtained from DIC measurements and the simulation are displayed at -1% of macroscopic strain in figures 7, 8 and 9, respectively. In this case, an overall good match between simulation and experiment is observed, which is confirmed by quantitative comparisons along horizontal and vertical lines (figure 10). The scattering is however a little bit more salient in the experiment, especially concerning the positive values of ε_{yy} in grain 2 (figure 7). Furthermore, the strongest localization of experimental strains in grains 3 and 7 is explained by the presence of a large kink band that cross both grains and which is perpendicular to the first basal glide direction (see figure 3). The presence of this kink band was experimentally confirmed by $\boldsymbol{c}$-axis misorientation measurements across grains 3 and 7. The average kink band $\boldsymbol{c}$-axis misorientation relative to the parent grain was about 6° in grain 7 and about 4° in grain 3.

4.3.3. Evolution and distribution of dislocation densities Figure 11 shows the average evolution of the different dislocation species ρ_m, ρ_f, ρ_{GND} and ρ_t summed over all slip systems and figure 12 their spatial distribution. It is noteworthy that the global GND density decreases after unloading. This decrease is caused by dislocations annihilation similarly to what happened during the reverse creep of the single crystals (see figure 5). Hence, it confirms the presence of reverse plasticity in the simulation. The mobile SSD density follows area that exhibit high plastic slip rates, as does the immobile SSD density. Due to their evolution equation (36), the latter also localize in multiple slip deforming area, *i.e.* around grain boundaries in the present simulation. As expected, the GND density starts to grow from triple junctions and grain boundaries and then progressively extends towards the interior of the grains (*e.g.*, see the dislocation pattern that extends from the triple junction between grains 3, 10 and 11 towards the interior of grain 11). Given the distribution of the total dislocation density, it is noteworthy

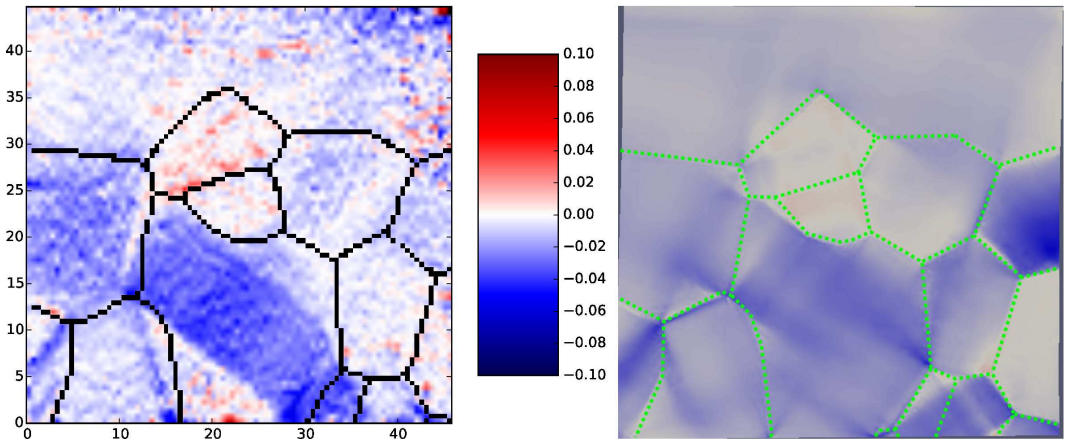

Figure 7. Distribution of strain ε_{yy} at -1% of macroscopic strain: DIC measurement (left) and RPMFDM (right). The initial positions of the grain boundaries are indicated in black (left) or in dotted green lines (right). The dimensions of the sample are given in mm.

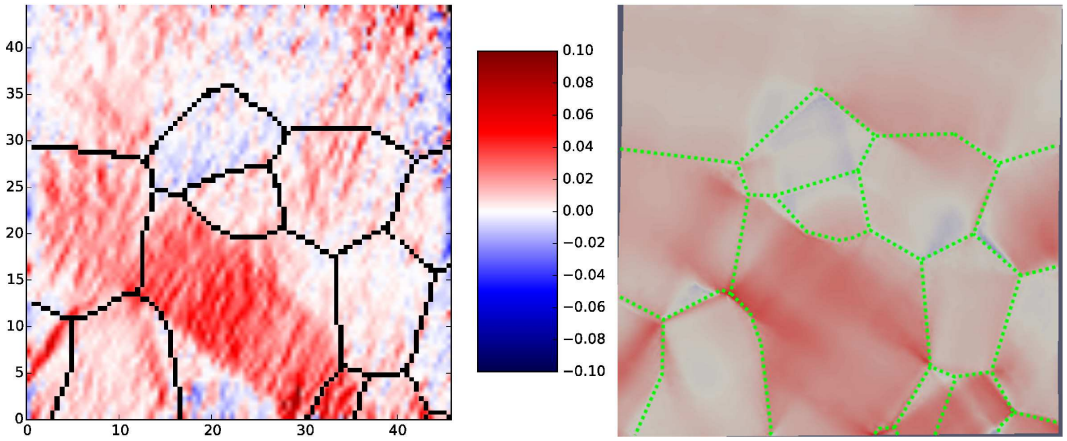

Figure 8. Distribution of strain ε_{xx} at -1% of macroscopic strain: DIC measurement (left) and RPMFDM (right). The initial positions of the grain boundaries are indicated in black (left) or in dotted green lines (right). The dimensions of the sample are given in mm.

that the dislocation mobility (see (33) and (34)) is strongly reduced close to some grain boundaries.

4.3.4. Observation of relaxation mechanisms From the observation of the specimen microstructure after deformation (figure 3), it can be inferred that grain boundary migration and grain nucleation also took place as relaxation mechanisms in addition to kink banding. These are common phenomena in ice after 1% macroscopic strain at high temperature. In particular, despite the local character of grain boundary motion, it can be asserted that (see figure 3):

- GB 1-2 $\rightarrow$ 1,

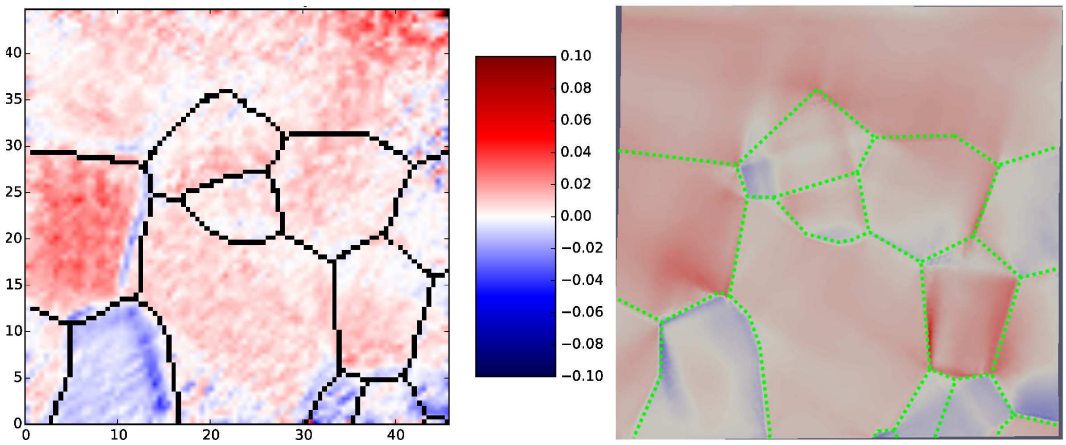

Figure 9. Distribution of strain ε_{xy} at -1% of macroscopic strain: DIC measurement (left) and RPMFDM (right). The initial positions of the grain boundaries are indicated in black (left) or in dotted green lines (right). The dimensions of the sample are given in mm.

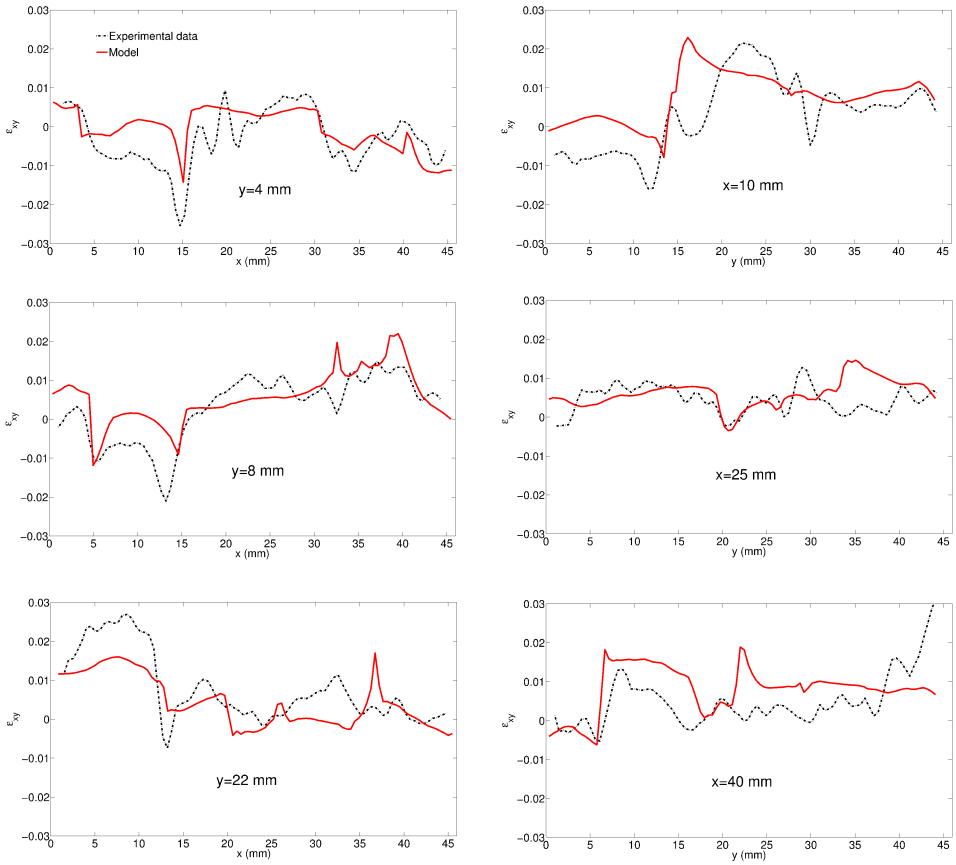

Figure 10. Quantitative comparisons of ε_{xy} between DIC measurement and RPMFDM along horizontal and vertical lines at -1% of macroscopic strain.

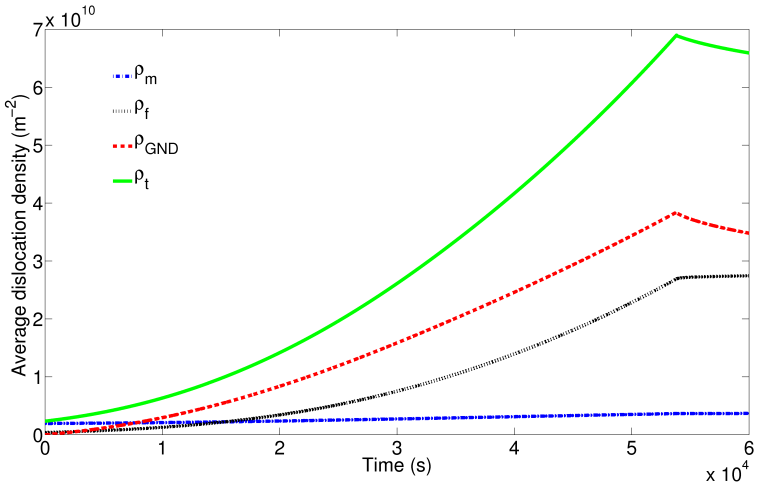

Figure 11. Evolution of the statistical mobile (ρ_m), immobile (ρ_f), GND (ρ_{GND}) and total (ρ_t) dislocation densities, summed over all slip systems and averaged over the specimen, during compression creep of the multi-crystal.

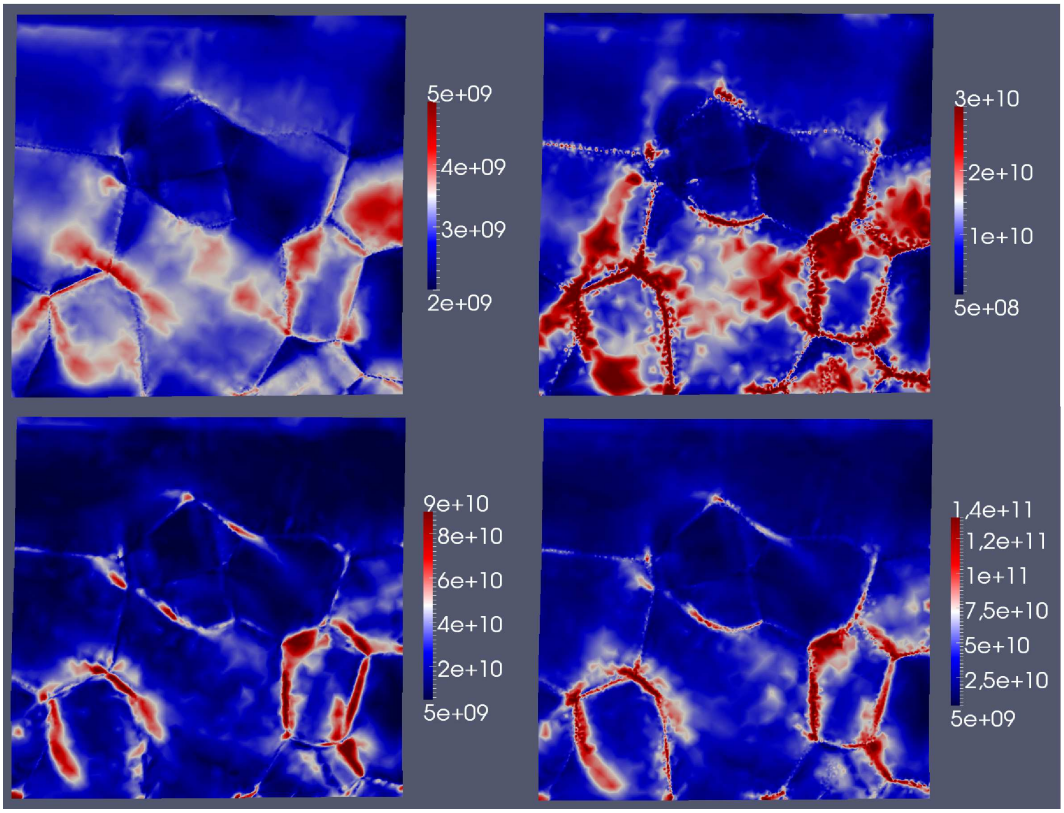

Figure 12. Distribution of the mobile SSD (ρ_m), immobile SSD (ρ_f), GND (ρ_{GND}) and total (ρ_t) dislocation densities in m^{-2}, summed over all slip systems, at -1% macroscopic strain (from left to right and top to bottom, respectively).

- GB 1-5 → 1,
- GB 4-7 → 7,
- GB 7-8 → 8,
- GB 8-9 → 8,

where the notation "GB i-j → i (or j)" means that the grain boundary between grains i and j has globally moved towards grain i (or j). Concerning, the boundary between grains 5 and 7, local migration took place but no global tendency is observed (figure 3). Furthermore, grain nucleation is visible around the triple junction between grains 1, 2 and 3 and the one between grains 3, 7 and 11 (figure 3).

5. Discussion

Experimental strain patterns are globally well retrieved by the simulation despite the observed presence of a large kink band which reinforces strain localization. As a matter of fact, the present model is not designed to fully account for the mechanism of kink band formation. However, it is very interesting to notice that the observed kink band position corresponds very well with an area of strong $\boldsymbol{c}$-axis misorientation predicted by the simulation (figure 13). What is particularly striking is the continuity predicted by the simulation of the $\boldsymbol{c}$-axis misorientation between grains 3 and 7. Moreover, figure 14 shows the distribution of screw and edge GND densities on the first basal slip system. Remarkably, it is seen that the area of the observed kink band is bounded by opposite densities of edge dislocations as it is expected from the theory [54, 62] and the observations [63, 64].

Besides, following recrystallization and grain boundary motion theories [65], the predicted dislocation distribution is perfectly consistent with the observed movements of grain boundary migration, *i.e.* the boundaries migrate from low dislocation density area towards high dislocation ones (see section 4.3.4 and figure 12). In addition, there is no considerable difference of dislocation density between grains 5 and 7 in agreement with the absence of a global migration tendency in this case. The observed moving boundaries also often coincide with predicted area of high lattice misorientation (figure 13) and strong gradient of elastic energy density (figure 15). Moreover, the triple junctions where grain nucleation is observed (see section 4.3.4) are characterized in the simulation by high GND densities (figure 12) and especially strong gradient of elastic energy density (figure 15). This last quantity seems the most relevant one to be correlated with grain nucleation.

So, the model seems to capture correctly the area with high stored elastic energy which are afterward relaxed by recrystallization mechanisms. However, as observed in [30] in ice, recrystallization processes are followed by a redistribution of local strain fields. The non-consideration of these mechanisms in the model may explain some of the differences noticed with the experience in the strain patterns distribution (figures 7, 8, 9 and10) and in the macroscopic behavior (figure 6). Disparity from the macroscopic

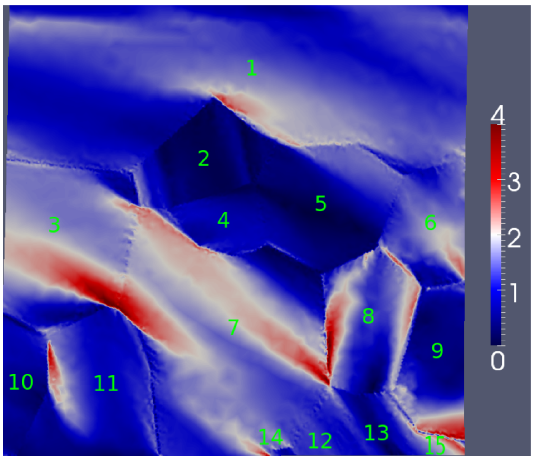

Figure 13. Distribution of the ***c***-axis misorientation in degrees in relation to the initial orientation at -1% of macroscopic strain.

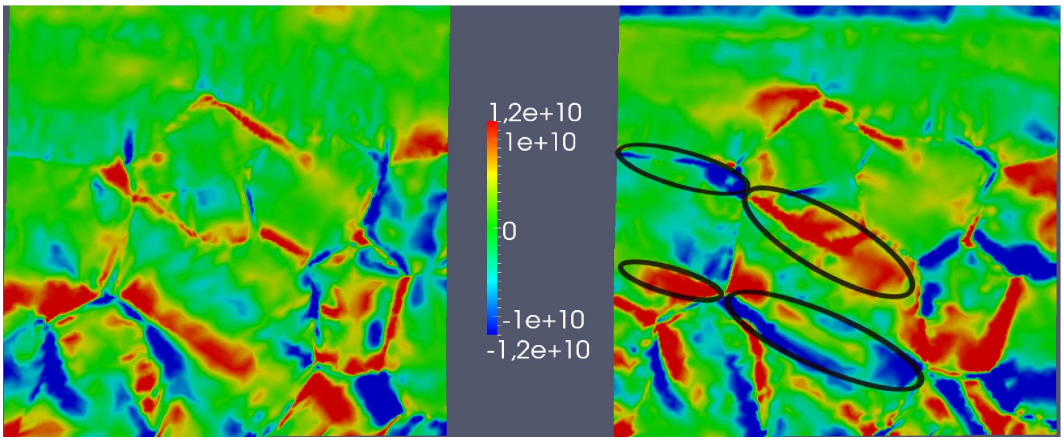

Figure 14. Distribution of screw (left) and edge (right) GND densities in m^{-2} on the first basal slip system at -1% macroscopic strain. The black circles indicate the presence of opposite edge dislocation densities in grains 3 and 7 that bound the observed kink band.

behavior may also partly result from not truly realistic initial and boundary conditions which are expected to affect even more the mechanical response since the sample is far from a Representative Volume Element (RVE). Still, the unrealistic creep acceleration seems to be correlated with the GND increase (figure 11), similarly to what was observed in the torsion tests. Actually, assuming that the total dislocation density scales almost like the GND density (see figure 11) the slipping rate $\dot{\gamma}^{(s)}$ would scale, in a first approximation, as ${\rho_{GND}^{(s)}}^{1-\frac{n^{(s)}}{2}}$ from (32), (33), (34), (35), *i.e.* $\dot{\gamma}^{(s)} \sim \sqrt{\rho_{GND}^{(s)}}$ for basal slip systems. Hence, there is a tendency that the basal slip rates increase with the growth of the GND densities. However, $\dot{\gamma}^{(s)}$ is also influenced by kinematic hardening through the evolution of the resolved shear stress $\tau^{(s)}$ that intervenes in the computation of the dislocation velocity $v^{(s)}$ (33). Kinematic hardening is indeed present in our simulation

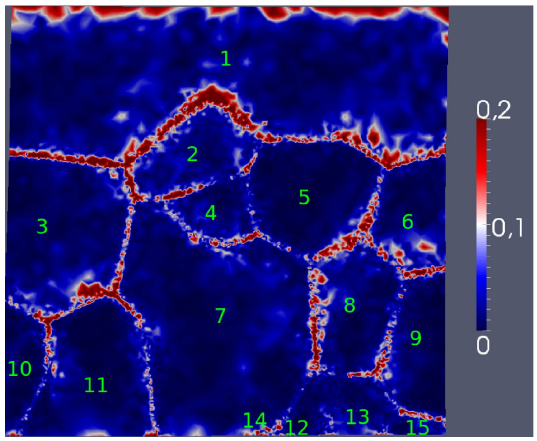

Figure 15. Distribution of the gradient of the elastic energy density in MJm^{-4} at -1% of macroscopic strain.

as it is illustrated in figures 16 and 17 where it is seen that, despite the absence of a phenomenological kinematic hardening term in the constitutive equations, back-stresses of the same order of magnitude than the applied resolved shear stresses are present. Figure 16 displays the distribution of the resolved shear stress on the first basal slip system, $\tau^{(1)}$, just after loading, at -1% of macroscopic strain, just before unloading and after unloading. By construction, $\tau^{(1)}$ is positive everywhere at the very beginning of the creep test (see section 3.1.3). In most places $\tau^{(1)}$ decreases and becomes even negative in some grains. As a consequence, $\tau^{(1)}$ is mostly negative after unloading, which explains the reverse plastic strain. Since the macroscopic stress remains constant during a creep test, the evolution of the resolved shear stresses on slip systems depicts the effect of the building up of an internal stress field or, in other words, the emergence of back-stresses on slip systems. As another illustration, figure 17 exhibits the evolution of back-stresses on the three basal systems averaged over the specimen. Because of lattice rotation, these mean back-stresses $\tau_{BS}^{(s)}$ were evaluated as follows:

$$\tau_{BS}^{(s)} = | < \tau^{(s)} > -\Sigma_u < R_{22}^{(s)} > |, \tag{43}$$

where $<>$ denotes spatial averaging over the specimen, Σ_u the applied uniaxial macroscopic stress ($-0.25MPa$ during loading and null at unloading) and $R_{22}^{(s)}$ the component 22 of the Schmid orientation tensor (see (19)). Figure 17 shows that the three mean back-stresses on the basal systems increase continuously during the loading creep and then decrease exponentially to zero during unloading.

This kinematic hardening is responsible for the reverse plasticity that was established after unloading in section 4.3. However, the rate of the reverse plasticity appears too small compared with the quasi-instantaneous inelastic reverse strain observed experimentally. Accordingly, the acceleration of the creep rate and the too small reverse strain both suggest that the level of kinematic hardening is not high enough in our simulation. This level notably depends on how is modeled the interactions

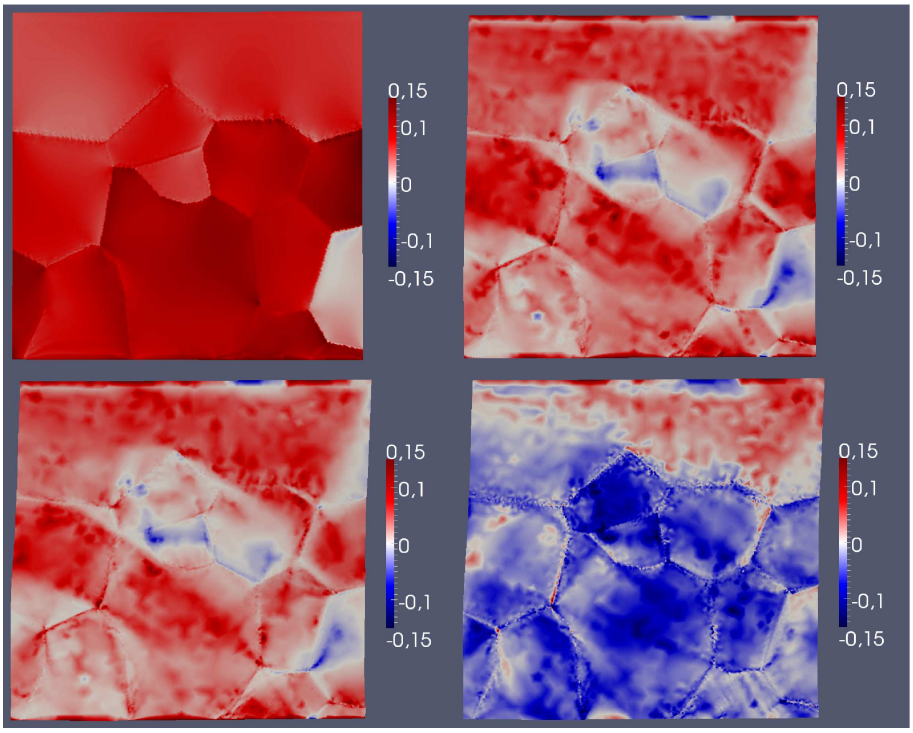

Figure 16. Distribution of the resolved shear stress in MPa on the basal slip system numbered 1, $\tau^{(1)}$, just after loading, at -1% of macroscopic strain, just before unloading at -1.9% of macroscopic strain and just after unloading (from left to right and top to bottom, respectively).

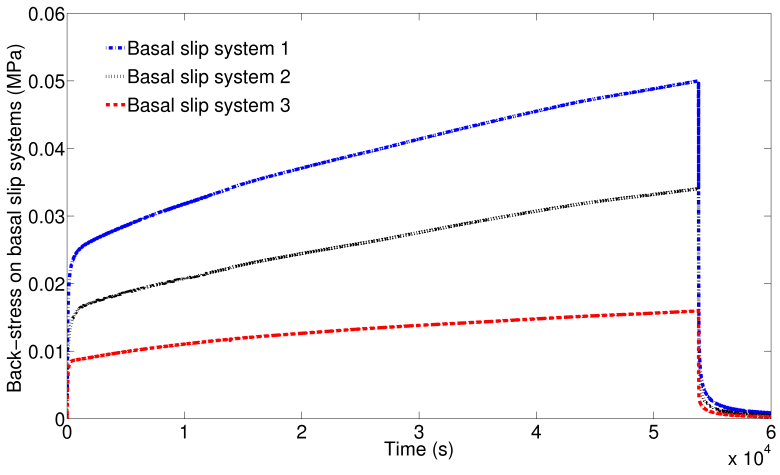

Figure 17. Evolution of the mean back-stress on basal slip systems as estimated by (43).

between dislocations and grain boundaries and how is resolved the transport at grain boundaries. Although the dislocation mobility is already strongly reduced around some grain boundaries (see section 4.3.3), the current simplified treatment can clearly be improved in future work as explained in section 3.1.3. In particular, the introduction of a phenomenological GND induced back-stress, as done for instance in [16, 18, 52, 55], could surely increase the recoverable viscoplastic deformation after unloading. Moreover, line tension effects are also not included in the present model but may be important at unloading. For instance, it was recently shown thanks to a higher order continuum dislocation theory that a global decrease of dislocation line curvature can produce a strong softening [27]. However, our simulated back-stresses on slip systems are already of the order of magnitude of the applied resolved shear stresses (figure 16 and figure 17) and thus new back-stresses could not be so much greater that the current ones since otherwise the sample would be in tension and not in compression during loading. Hence, given the difference of strain jumps, it is likely that even such an improved setting may be not sufficient to capture the totality of the reverse inelastic strain. As mentioned, the kinetics at unloading is strongly different between observation and modeling. In order to explain such a difference, the dislocation velocity law used (33) can also be put into question. Indeed, the model uses the same constitutive law as during loading, while the fast strain decrease observed suggests that dislocations move back with abnormally huge velocity when the imposed stress is removed. This could be linked to the well known avalanche-like behavior of dislocations in ice [66, 67] and/or to inertial effects.

6. Conclusions

A Reduced Phenomenological model of Mesoscopic Field Dislocation Mechanics that accounts for the transport of GND densities on slip systems was developed. It was applied to the simulation of the forward and reverse torsion creep behavior of two single crystals of ice with different sizes and temperatures and to the compression creep behavior of a multi-crystal of ice followed by unloading. With the same set of parameters, good agreement was obtained between the experimental and simulated forward and reverse creep curves of the single crystals, as well as with the 2D strain fields obtained by DIC on the multi-crystal and the ones simulated. It was shown also that this model is capable of simulating significant kinematic hardening without considering a phenomenological back-stress in the dislocation velocity constitutive law. However, in the multi-crystal compression test, the inelastic strain jump at unloading was small compared to the one observed, suggesting that mechanisms that are not included in the model, like inertial and/or line tension effects, might actually prevail in the building up of the back-stresses responsible for the inelastic reverse strain jump. Besides, the compression of the multi-crystal was characterized by the formation of a large kink band across two grains, grain boundary migration at several places and some grains nucleation. Remarkably, the kink band position corresponded very well with an area of strong $\boldsymbol{c}$-axis misorientation predicted by the model and was also bounded

by opposite densities of edge dislocations, in agreement with kink banding theory and characterization [54, 62–64]. Furthermore, grain boundary migration was observed to happen from predicted low dislocation density area towards high dislocation ones, also in agreement with the grain boundary motion theory [65]. The observed moving boundaries were also often coincident with predicted area of high lattice misorientation and strong gradient of elastic energy density. Lastly, the triple junctions where nucleation were observed were also characterized in the simulation by high GND density and especially strong gradient of elastic energy density. These different observations suggest that the developed model still correctly captures the main physical mechanisms leading to the building up of an internal stress field and dislocation patterns. In particular, it shows the relevance of using a continuum theory of polarized dislocations per slip systems to study the onset of relaxation mechanisms like kink banding, grain boundary migration and grain nucleation. In future work, such a theory could certainly help to provide nucleation and migration criteria.

7. Acknowledgements

The authors are grateful to the French National Research Agency (ANR) for financial support under contract "DREAM" (ANR-13-BS09-0001-03). This project is also supported by INP-Grenoble and the University Grenoble-Alpes in the frame of proposal called "Grenoble Innovation Recherche AGIR".

8. Appendix

Following Acharya [11], the driving force for GND on the slip system (s) is

$$\boldsymbol{f} = \boldsymbol{X}\left(\boldsymbol{\sigma}\boldsymbol{\alpha}^{(s)}\right), \tag{A.1}$$

where $\boldsymbol{X}$ is the third-order alternating tensor as defined in section 2. It is actually analogous to the Peach-Koehler force that is applied to a discrete dislocation line. In order to estimate the contribution of the GND to the slipping rates $\dot{\gamma}^{(s)}$, we consider that $\boldsymbol{b}^{(s)}$ and $\boldsymbol{b}^{\boldsymbol{u}*(s)}$ are close to each other and that $J = 1$ (see section 3.2). In the orthonormal frame $\left(\boldsymbol{b}^{\boldsymbol{u}*(s)}, \boldsymbol{n}^{\boldsymbol{u}*(s)}, \boldsymbol{k}^{\boldsymbol{u}*(s)}\right)$ associated to the slip system (s), the driving force $\boldsymbol{f}$ can thus be approximated as:

$$\boldsymbol{f} = \begin{pmatrix} \sigma_{12}\alpha^{(s)}_{edge} \\ \sigma_{13}\alpha^{(s)}_{screw} - \sigma_{11}\alpha^{(s)}_{edge} \\ -\sigma_{12}\alpha^{(s)}_{screw} \end{pmatrix}. \tag{A.2}$$

The terms $\sigma_{13}\alpha^{(s)}_{screw}$ and $-\sigma_{11}\alpha^{(s)}_{edge}$ represent driving forces for cross-slip of screw dislocations and climb of edge dislocations, respectively, that is for out-of-plane motions [11]. The two remaining terms correspond to driving forces for glide of edge and screw components, that is for in-plane motions. It would be irrelevant to account for climb and cross-slip through the transport equations (26) in our simulations which intend to

model areas of several centimeters. Hence, only in-plane motions are taken into account. The GND velocity is then assumed proportional to the in-plane part of the driving force, which is the most simple way to ensure positive dissipation [11]:

$$\boldsymbol{V}^{(s)} = v^{(s)} \begin{pmatrix} \frac{\alpha_{edge}^{(s)}}{\sqrt{{\alpha_{screw}^{(s)}}^2 + {\alpha_{edge}^{(s)}}^2}} \\ 0 \\ -\frac{\alpha_{screw}^{(s)}}{\sqrt{{\alpha_{screw}^{(s)}}^2 + {\alpha_{edge}^{(s)}}^2}} \end{pmatrix}, \tag{A.3}$$

where $v^{(s)}$, the velocity magnitude given by (33), is of the same sign as σ_{12}. Indeed, in the frame associated to the slip system (s), σ_{12} coincides with the resolved shear stress $\tau^{(s)}$ (25) given our assumptions. Moreover, the contribution of GND to the plastic slipping rate $\dot{\gamma}_{GND}^{(s)}$ also coincides with the component 12 of the plastic distortion rate $\left(\boldsymbol{\alpha}^{(s)} \times \boldsymbol{V}^{(s)}\right)_{12}$ [10]:

$$\dot{\gamma}_{GND}^{(s)} = \alpha_{edge}^{(s)} V_1^{(s)} - \alpha_{screw}^{(s)} V_3^{(s)} = \sqrt{{\alpha_{screw}^{(s)}}^2 + {\alpha_{edge}^{(s)}}^2}\, v^{(s)}. \tag{A.4}$$

Supplementing (A.4) with the contribution of mobile SSD, $\rho_m^{(s)} b^{(s)} v^{(s)}$, the total slipping rate $\dot{\gamma}^{(s)}$ can finally be expressed in the form of a generalized Orowan relation as given by (32).

Appendix B. References

[1] P. Duval, M.F. Ashby, and I. Anderman. Rate-controlling processes in the creep of polycrystalline ice. *J. Phys. Chem.*, 87:4066–4074, 1983.

[2] M.F. Ashby. The deformation of plastically non-homogeneous materials. *Phil. Mag.*, 21:399–424, 1970.

[3] M. Montagnat, J.R. Blackford, S. Piazolo, L. Arnaud, and R.A. Lebensohn. Measurements and full-field predictions of deformation heterogeneities in ice. *Earth Planet. Sc. Lett.*, 305:153–160, 2011.

[4] E. Kröner. *Kontinuumstheorie der Versetzungen und Eigenspannungen*. Springer Verlag, Berlin, 1958.

[5] B.A. Bilby, R. Bullough, and E. Smith. Continuous distributions of dislocations: a new application of the methods of non-riemannian geometry. *Proc. Roy. Soc. London A*, 231:263–273, 1955.

[6] T. Mura. Continuous distribution of moving dislocations. *Phil. Mag.*, 89:843–857, 1963.

[7] J. R. Willis. Second order effects of dislocations in anisotropic crystalss. *International Journal of Engineering Science*, 5:171–190, 1968.

[8] J.F. Nye. Some geometrical relations in dislocated crystals. *Acta Metall.*, 1:153–162, 1953.

[9] A. Acharya and J.L. Bassani. Lattice incompatibility and a gradient theory of crystal plasticity. *J. Mech. Phys. Solids*, 48:1565–1595, 2000.

[10] A. Acharya. A model of crystal plasticity based on the theory of continuously distributed dislocations. *J. Mech. Phys. Solids*, 49:761–784, 2001.

[11] A. Acharya. Driving forces and boundary conditions in continuum dislocation mechanics. *Proc. R. Soc. Lond. A*, 459:1343–1363, 2003.

[12] S.N. Varadhan, A.J. Beaudoin, and C. Fressengeas. Dislocation transport using an explicit Galerkin/least-squares formulation. *Model. Simul. Mater. Sci. Eng.*, 14:1245–1270, 2006.

[13] A. Acharya and A. Roy. Size effects and idealized dislocation microstructure at small scales: Predictions of a Phenomenological model of Mesoscopic Field Dislocation mechanics: Part I. *J. Mech. Phys. Solids*, 54:1687–1710, 2006.

[14] A. Roy and A. Acharya. Size effects and idealized dislocation microstructure at small scales: Predictions of a Phenomenological model of Mesoscopic Field Dislocation Mechanics: Part II. *J. Mech. Phys. Solids.*, 54:1711–1743, 2006.

[15] A. Roy, S. Puri, and A. Acharya. Phenomenological mesoscopic field dislocation mechanics, lower-order gradient plasticity, and transport of mean excess dislocation density. *Modelling Simul. Mater. Sci. Eng.*, 15:167–180, 2007.

[16] V. Taupin, S. Varadhan, J. Chevy, C. Fressengeas, A.J. Beaudoin, M. Montagnat, and P. Duval. Effects of size on the dynamics of dislocations in ice single crystals. *Phys. Rev. Lett.*, 99:155507 (1–4), 2007.

[17] T. Richeton, G.F. Wang, and C. Fressengeas. Continuity constraints at interfaces and their consequences on the work hardening of metal-matrix composites. *J. Mech. Phys. Solids*, 59:2023–2043, 2011.

[18] S. Puri, A. Das, and A. Acharya. Mechanical response of multicrystalline thin films in mesoscale field dislocation mechanics. *J. Mech. Phys. Solids*, 59:2400–2417, 2011.

[19] V. Taupin, S. Berbenni, and C. Fressengeas. Size effects on the hardening of channel-type microstructures: A field dislocation mechanics-based approach. *Acta Mater.*, 60:664–673, 2012.

[20] A. Acharya. Constitutive analysis of finite deformation field dislocation mechanics. *J. Mech. Phys. Solids*, 52:301–316, 2004.

[21] A. Arsenlis and D.M. Parks. Crystallographic aspects of geometrically-necessary and statistically-stored dislocation density. *Acta Mater.*, 47:1597–1611, 1999.

[22] A. Arsenlis and D.M. Parks. Modeling the evolution of crystallographic dislocation density in crystal plasticity. *J. Mech. Phys. Solids*, 50:1979–2009, 2002.

[23] A. Arsenlis, D.M. Parks, R. Becker, and V.V. Bulatov. On the evolution of crystallographic

dislocation density in non-homogeneously deforming crystals. *J. Mech. Phys. Solids*, 52:1213–1246, 2004.

[24] K.S. Cheong and E. Busso. Discrete dislocation density modelling of single phase fcc polycrystal aggregates. *Acta Mater.*, 52:5665–5675, 2004.

[25] A. Ma, F. Roters, and D. Raabe. A dislocation density based constitutive model for crystal plasticity FEM including geometrically necessary dislocations. *Acta Mater.*, 54:2169–2179, 2006.

[26] A. Ma, F. Roters, and D. Raabe. On the consideration of interactions between dislocations and grain boundaries in crystal plasticity finite element modeling Theory, experiments, and simulations. *Acta Mater.*, 54:2181–2194, 2006.

[27] T. Hochrainer, S. Stanfeld, M. Zaiser, and P. Gumbsch. Continuum dislocation dynamics: Towards a physical theory of crystal plasticity. *J. Mech. Phys. Solids*, 63:167–178, 2014.

[28] H. Hernández, T.J. Massart, R.H.J. Peerlings, and M.G.D. Geers. Towards an unconditionally stable numerical scheme for continuum dislocation transport. *Modelling Simul. Mater. Sci. Eng.*, 23:085013 (1–23), 2015.

[29] F. Grennerat, M. Montagnat, O. Castelnau, P. Vacher, H. Moulinec, P. Suquet, and P. Duval. Experimental characterization of the intragranular strain field in columnar ice during transient creep. *Acta Mater.*, 60:3655–3666, 2012.

[30] T. Chauve, M. Montagnat, and P. Vacher. Strain field evolution during dynamic recrystallization nucleation; a case study on ice. *Acta Mater.*, 101:116–124, 2015.

[31] R. Hill and J.R. Rice. Constitutive analysis of elastic-plastic crystals at arbitrary strain. *J. Mech. Phys. Solids*, 20:401–413, 1972.

[32] R.J. Asaro. Crystal plasticity. *J. Appl. Mech.*, 50:921–934, 1983.

[33] D. Peirce, R.J. Asaro, and A. Needleman. Material rate dependence and localized deformation in crystalline solids. *Acta Metall.*, 31:1951–1976, 1983.

[34] Y. Huang. A user material subroutine incorporating single crystal plasticity in the Abaqus finite element program. *Harvard University Cambridge, Massachusetts*, pages 1–21, 1991.

[35] A. Acharya. Jump condition for GND evolution as a constraint on slip transmission at grain boundaries. *Phil. Mag.*, 87:1349–1359, 2007.

[36] S. Ahmad and R.W. Whitworth. Dislocation motion in ice: a study by synchroton X-ray topography. *Philos. Mag. A*, 57:749–766, 1988.

[37] M. Montagnat, J. Weiss, P. Duval, H. Brunjail, and J.G. Sevillano. The heterogeneous nature of slip in ice single crystals deformed under torsion. *Philos. Mag.*, 86:4259–4270, 2011.

[38] Y. Estrin and L. P. Kubin. Local strain hardening and nonuniformity of plastic deformation. *Acta Metall.*, 34:2455–2466, 1986.

[39] C. Shearwood and R. Withworth. The velocity of dislocations in ice. *Phil. Mag.*, 64:289–302, 1991.

[40] Y. Okada, T. Hondoh, and S. Mae. Basal glide of dislocations in ice observed by synchrotron radiation topography. *Phil. Mag.*, 79:2853–2868, 1999.

[41] D.J. Bammann and E.C. Aifantis. On a proposal for a continuum with microstructure. *Acta Mech.*, 45:91–121, 1982.

[42] P. Franciosi, M. Berveiller, and A. Zaoui. Latent hardening in copper and aluminium single crystals. *Acta Metall.*, 28:273–283, 1980.

[43] L. Kubin, B. Devincre, and T. Hoc. Modeling dislocation storage rates and mean free paths in face-centered cubic crystals. *Acta Mater.*, 56:6040–6049, 2008.

[44] B. Devincre. Dislocation dynamics simulations of slip systems interactions and forest strengthening in ice single crystal. *Phil. Mag.*, 93:235–246, 2013.

[45] O. Castelnau, P. Duval, M. Montagnat, and R. Brenner. Elastoviscoplastic micromechanical modeling of the transient creep of ice. *J. Geophys. Res.*, 113:B11203 1–14, 2008.

[46] Z. Shen, R.H. Wagoner, and W.A.T.Clark. Dislocation and grain boundary interactions in metals. *Acta Metall.*, 36:3231–3242, 1988.

[47] T.C. Lee, I.M. Robertson, and H.K. Birnbaum. TEM in situ deformation study of the interaction

of lattice dislocations with grain boundaries in metals. *Phil. Mag. A*, 62:131–153, 1990.

[48] L.C. Lim and R. Raj. Interaction between lattice and garin boundary dislocations and their role in the mechanical properties of interfaces. *J. Phys. Colloq. C4*, 46:581–595, 1985.

[49] P. Gudmundson. A unified treatment of strain gradient plasticity. *J. Mech. Phys. Solids*, 52:1379–1406, 2004.

[50] L.P. Evers, D.M. Parks, W.A.M. Brekelmans, and M.G.D. Geers. Crystal plasticity model with enhanced hardening by geometrically necessary dislocation accumulation. *J. Mech. Phys. Solids*, 50:2403–2424, 2004.

[51] K.E. Aifantis, W.A. Soer, J.Th.M. De Hosson, and J.R. Willis. Interfaces within strain gradient plasticity: Theory and experiments. *Acta Mater.*, 54:5077–5085, 2006.

[52] C.J. Bayley, W.A.M. Brekelmans, and M.G.D. Geers. A comparison of dislocation induced back stress formulations in strain gradient crystal plasticity. *Int. J. Sol. Struct.*, 43:7268–7286, 2006.

[53] M.E. Gurtin. A theory of grain boundaries that accounts automatically for grain misorientation and grain-boundary orientation. *J. Mech. Phys. Solids*, 56:640–662, 2008.

[54] H.-J. Chang, A. Gaubert, M. Fivel, S. Berbenni, O. Bouaziz, and S. Forest. Analysis of particle induced dislocation structures using three-dimensional dislocation dynamics and strain gradient plasticity. *Comp. Mater. Science*, 52:33–39, 2012.

[55] P.R.M. van Beers, G.J. McShane, V.G. Kouznetsova, and M.G.D. Geers. Grain boundary interface in strain gradient crystal plasticity. *J. Mech. Phys. Solids*, 61:2659–2679, 2013.

[56] F. Hecht. New development in freefem++. *J. Num. Math.*, 20:251–266, 2012.

[57] D. Peirce, C.F. Shih, and A. Needleman. A tangent modulus method for rate dependent solids. *Comput. Struct.*, 18:875–887, 1984.

[58] J. Chevy. *Viscoplasticité et Hétérogénéités de déformation du monocristal de glace : expériences et simulations*. PhD thesis, Institut Polytechnique de Grenoble, 2008.

[59] C.J. Wilson, D.S. Russell-head, and H.M. Sim. The application of an automated fabric analyzer system to the textural evolution of folded ice layers in shear zones. *Ann. Glaciol.*, 37:7–17, 2003.

[60] M. Montagnat, T. Chauve, F. Barou, A. Tommasi, B. Beausir, and C. Fressengeas. Analysis of dynamic recrystallization of ice from EBSD orientation mapping. *Front. Earth Sci.*, 3:1–11, 2015.

[61] P.H. Gammon, H. Kiefte, M.J. Clouter, and W.W. Denner. Elastic constants of artificial and natural ice samples by Brillouin spectroscopy. *J. Glaciol.*, 29:433–460, 1983.

[62] F.C. Frank and A.N. Stroh. On the theory of kinking. *Proc. Phys. Soc. Sect. B*, 65:811–821, 1952.

[63] M. Yamasaki, K. Hagihara, S. i. Inoue, J.P. Hadorn, and Y. Kawamura. Crystallographic classification of kink bands in an extruded MgZnY alloy using intragranular misorientation axis analysis. *Acta Mater.*, 61:2065–2076, 2013.

[64] S. Piazolo, M. Montagnat, F. Grennerat, H. Moulinec, and J. Wheeler. Effect of local stress heterogeneities on dislocation fields: Examples from transient creep in polycrystalline ice. *Acta Mater.*, 90:303–309, 2015.

[65] J.E. Bailey and P.B. Hirsch. The recrystallization process in some polycrystalline metals. *Proc. R. Soc. A*, 267:11–30, 1962.

[66] M. C. Miguel, A. Vespignani, S. Zapperi, J. Weiss, and J. R. Grasso. Intermittent dislocation flow in viscoplastic deformation. *Nature*, 410:667–671, 2001.

[67] T. Richeton, J. Weiss, and F. Louchet. Breakdown of avalanche critical behaviour in polycrystalline plasticity. *Nat. Mater.*, 4:465–469, 2005.